Three-scale multiphysics finite element framework (FE^3) modelling fault reactivation

Martin Lesueur^{a,*}, Thomas Poulet^b and Manolis Veveakis^a

^{a}*Civil and Environmental Engineering, Duke, Durham, NC 27708-0287, USA*
^{b}*CSIRO Mineral Resources, 26 Dick Perry Avenue, Kensington, WA 6151, Australia*

ARTICLE INFO

ABSTRACT

Fluid injection or production in petroleum reservoirs affects the reservoir stresses such that it can even sometime reactivate dormant faults in the vicinity. In the particular case of deep carbonate reservoirs, faults can also be chemically active; chemical dissolution of the fault core can transform an otherwise impermeable barrier to a flow channel. Due to the scale separation of the fault compared to the reservoir, implementation of highly non-linear multiphysics processes for the fault, needed for such phenomenon, is not compatible with simpler poromechanics controlling the reservoir behaviour. This contribution presents a three-scale finite element framework using the REDBACK simulator to account for those multiphysics couplings in faults during fluid production. This approach links the reservoir (km) scale - implementing poromechanics both for the fault interface and its surrounding reservoir - with the fault at the meso-scale (m) - implementing a THMC reactivation model - and the micro-scale (μm) - implementing a hydro-chemical model on meshed μCT-scan images. This model can explain the permeability increase during fault reactivation and successfully replicate fault activation, evolution and deactivation features, predicted by common fault reactivation models, yet with continuous transitions between phases. The multiscale coupling allows to resolve the heterogenous propagation of the fault slip which proves to be independent of the initial highest slip tendency location. The influence of the rock microstructure on fault and reservoir behaviour is quantified in a simulation where a hydraulically imperceptible difference in the microstructure's geometry results in a different duration of the reactivation event at the macro-scale. We demonstrate the advantage of dynamically upscaled laws compared to empirical laws as we capture permeability hysteresis during dissolution/precipitation of the fault.

Contents

*Corresponding author
✉ martin.lesueur@duke.edu (M. Lesueur)
ORCID(s): 0000-0001-9535-2268 (M. Lesueur); 0000-0001-7351-3083 (T. Poulet)

1. Introduction

Faults are characteristic features of subsurface, with their activity being key a key subject of several disciplines including seismology, mining and energy engineering, landslides etc. They can be fluid conduits or barriers making them critical to compartmentalisation of the crust's resources, when flow is prevented across 'sealed' boundaries in the reservoir, usually faults. This commonly exaggerated description actually refers to formations of very low permeability, at the reservoir boundaries, that reduce cross-flow to infinitesimally slow rates (Jolley, Fisher and Ainsworth, 2010), allowing fluids and pressures to equilibrate across a boundary over geological timescales, but acting as seals over production time-scales (Wibberley, Yielding and Di Toro, 2008). As such, during energy operations, direct contact with faults is usually actively avoided throughout the drilling phase. Nonetheless, interferences of wells with a side-seal fault during injection or stimulation phases remain frequent, with induced stresses large enough to reactivate nearby dormant faults. The detailed database of Wilson, Foulger, Gluyas, Davies and Julian (2017) of recorded induced seismicity around the world exposes indeed how frequently these events occur, with currently a growing concern in Oklahoma, for instance, about the multiplication of such events (Keranen, Weingarten, Abers, Bekins and Ge, 2014).

Interestingly, following the reactivation of a fault, pressure equilibration between the two sides of the fault can sometimes be observed. A sealing fault then becomes a flow channel, at least temporarily and can render a reservoir completely inoperable at engineering time-scales, irrespective of the type of application. This process of a fault reactivating with simultaneous permeability increase is characteristic of a *fault-valve* behaviour, as described in the seminal work of Sibson, Robert and Poulsen (1988). The accumulation of fluids at the fault builds up the stress that eventually forces the fault to reactivate. The fluid is discharged along the fault for a short period of time, usually followed by a self-healing of the fault due to mineral precipitation of those flowing fluids in the fault veins. The modelling of this complex phenomenon -including mechanical, chemical, hydraulic and potential thermal feedbacks) during petroleum production is announced as one of the modern challenges in geomechanics, particularly in Brazil for instance, where "*reactivation must be avoided at any cost*" (Serra de Souza and Lima Falcão, 2015).

Current state-of-the-art considerations in fault reactivation modelling usually start with a poroelastic model describing the reservoir, in order to first account for the stress changes at the fault due to the pressure depletion induced by the fluid production. In such an approach, the fault is treated as a frictional interface, and reactivation triggering follows the coulomb failure criterion (Jaeger, 2007), allowing to determine the location and timing of reactivation events. Furthermore, the resulting evolution of the slip rate can be modelled with a rate-and-state (Dieterich, 1979) or a linear slip-weakening law (Andrews, 1976). This purely mechanical framework has proven capable of matching multiple case studies already (e.g. Cappa and Rutqvist, 2011), but more physical effects remain to be accounted for, like temperature effects for instance, since thermal pressurisation was shown to be a predominant term in the weakening of the fault (Rice, 2006). Temperature, however, is rarely modelled during fault reactivation due to the complexity of handling its
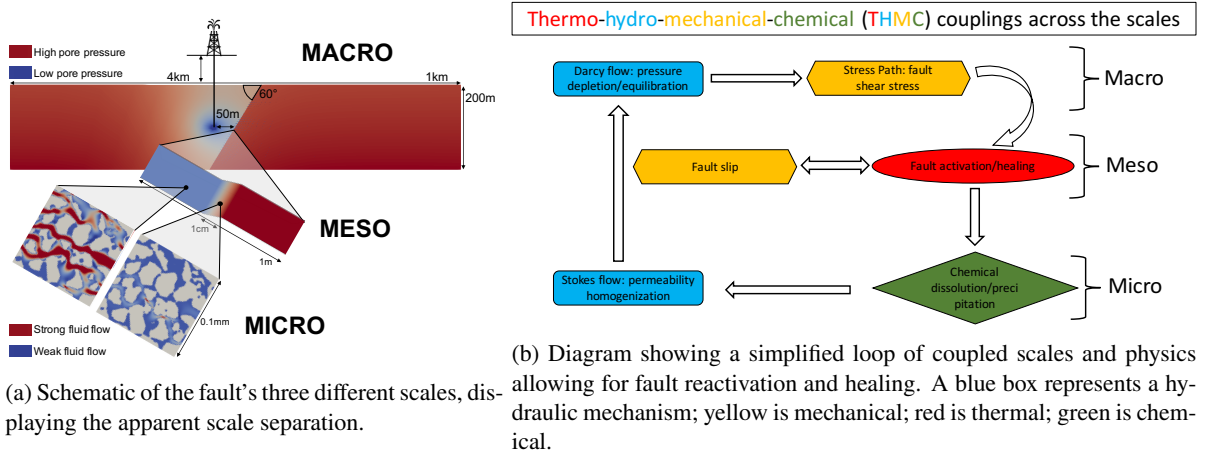
impact at the various time scales involved for the stress, pore pressure and heat propagations, around the fault and in the reservoir. Accounting for temperature is therefore more complex than directly implementing an empirical interface law and requires multiscale modelling. Following the same concept, the interface law at the reservoir-scale can be enriched by including different information such as the multi-porosity/multi-permeability nature of porous media from the study of Wang and Sun (2018).

Regardless of the degree of realism reached for the mechanical slip, a notable limitation to both the Coulomb Failure Stress and Rate and State approaches is their inability to explain effectively a permeability increase concomitant to the fault's reactivation. In order to couple the reactivation to an increase of permeability, faults are commonly characterised by the aperture of the fractures, which is linked to the normal and shear strain (Olsson and Barton, 2001). This theory allows to fit multiple case studies (e.g. Bandis, Lumsden and Barton, 1983; Olsson and Barton, 2001), however it suffers from a difficult calibration process and does not provide an explanation for the healing of the fault since the accumulation of shear strain is an irreversible process. In addition, studies have shown that purely mechanical models cannot model orders of magnitude of permeability increase observed in some case studies (Zhang, Clennell, Delle Piane, Ahmed and Sarout, 2016; Cleary, Pereira, Lemiale, Delle Piane and Clennell, 2015) and Zhang et al. (2016) suggest another physical explanation for the increase of permeability: chemical dissolution.

In this work, we aim at modelling the multiscale and multiphysics nature of fault reactivation with permeability evolution, restricting ourselves to fault reactivation events involving fluid-producing chemical reactions. In such cases, the ductile nature of the process yields results that depend mainly on the physics of the processes involved, making the whole process much more tractable than for brittle events. Such faults are treated as elasto-viscoplastic domains, with mineralogies that are prone to dissolution/precipitation reactions triggered by temperature increase during slip (i.e. chemically active). The reactivation of such chemically active faults can be modelled with the chemical shear zone model of Alevizos, Poulet and Veveakis (2014), which extends the rate and state law for ductile rocks that are temperature and rate sensitive in a chemical environment. That theory has been successfully applied to explain the stick-slip behaviour of subduction zones (Veveakis, Poulet and Alevizos, 2014), as well as spatial features of exhumed carbonate thrusts (Poulet, Veveakis, Herwegh, Buckingham and Regenauer-Lieb, 2014b), all requiring specific temperature conditions involving depths of several kilometres (Poulet et al., 2014b) for episodic reactivation events to take place. The same model can also lead to one-off events much more easily, in environments with much lower forces involved (Poulet, Veveakis, Regenauer-Lieb and Yuen, 2014a). Given the fact that more than 50% of global gas reserves are estimated to be held in carbonate reservoirs (Burchette, 2012), this chemical type of fault reactivation actually represents a major case study that will only become more relevant as reservoir operations are getting increasingly deeper. Considering this type of reactivation, a substantial permeability increase can get generated during fault slip by chemical dissolution, and the healing of the fault after discharge can easily be explained with a precipitation sealing mechanism.

The relationship between chemical dissolution or precipitation and permeability is commonly modelled with an empirical law between porosity and permeability, Kozeny-Carman arguably being the most famous one. While the law provides a satisfactory fit for most cases, its limitations are well-known (Scheidegger, 1974) and particularly for the case of fault reactivation, does not work well using porosity changes stemming from shear deformations (Wong and Li, 2001). The reason is that porosity only represents one of the possible variables to characterise the microstructure and can therefore not capture all microstructural effects effectively. Arns (2009) focused on deriving more of those characteristic numbers that can be obtained from micro Computed Tomography (μCT) images. The other possible approach is not to reduce the information contained in the microstructure. Indeed, CT technology has reached a level of maturity such that research based on CT-scan images has moved from pure visualisation to quantified characterisation, opening the door to physical modelling. Access to digital porous rocks at high resolution has enabled the development of computational approaches to complement - with the goal of ultimately replace - more expensive laboratory experiments. Such numerical approaches resolve directly the transport equations in micro-tomographic images (Mostaghimi, Blunt and Bijeljic, 2012) and remove the uncertainties introduced by the empirical nature of the scaling factors used to fit the experimental data (Andrä, Combaret, Dvorkin, Glatt, Han, Kabel, Keehm, Krzikalla, Lee, Madonna, Marsh, Mukerji, Saenger, Sain, Saxena, Ricker, Wiegmann and Zhan, 2013). Indeed, in order to quantify the effect of chemical alterations on permeability, the fluid flow needs to be fully resolved on the deformed microstructure, and then homogenised to a permeability value.

To account for the role of the outer domain (reservoir) on the stresses acting on the fault, we use a multiscale approach with three scales of consideration, displayed in Fig. 1a: At the macro-, or reservoir scale (km) , the reservoir is modelled as a poro-elastic medium and the fault is treated as a frictional interface, with its frictional response calculated at a separate lower-scale simulation; at the meso-, or fault scale (m), the fault is considered as a thermo-

(a) Schematic of the fault's three different scales, displaying the apparent scale separation.

(b) Diagram showing a simplified loop of coupled scales and physics allowing for fault reactivation and healing. A blue box represents a hydraulic mechanism; yellow is mechanical; red is thermal; green is chemical.

Figure 1: Schematic of the multiscale framework in terms of (a) scale separation and (b) coupled processes.

hydro-chemo-elasto-visco-plastic domain; the micro-scale (μm) is added for the refinement of the permeability evolution, implementing a hydro-chemical model on meshed μCT-scan images. The macro and meso scales are solved with FEM as well, as commonly done for continuum modelling of mechanical problems. The use of a common platform, REDBACK, for this FE³ framework is enabled by the use of the *multiapp* capability of MOOSE that manages the distribution of embedded applications (called *subapps*) automatically and the transfer functions that can pass information to each *subapp*.

We start by introducing the implementation of this three-scale framework, with the governing laws at each scale (macro, meso and micro in Sec. 2, 3 and 5 respectively) as well as the coupling schemes between them (macro/meso and meso/micro in Sec. 4 and 6 respectively). Sec. 7 links all elements by applying the framework to a generic geological scenario of induced chemical fault reactivation. Eventually Sec. 8 summarises how all the components were successfully put together and highlights the main findings of this contribution.

2. Modelling the fault at the physical scale (meso)

The system of equations controlling the behaviour of the fault at the centimetre to metre scale (Figure 2) is derived in details in Alevizos et al. (2014) and briefly summarized in this section. In essence, the fault is initially in a creeping regime, with negligible displacement at engineering time scales, yet produces heat from internal friction which can lead to thermal runaway (Regenauer-Lieb and Yuen, 1998). The sudden increase in temperature from the fault reactivation triggers a calcite decomposition reaction which dramatically increases the permeability of the fault, allowing pressure equilibration across. This evolution can be described through the mass, momentum and energy balance equations with a set of constitutive laws.

2.1. Physical formulation

The mechanical deformation is solved by the momentum balance under quasi-static assumption, leading to the evolution of effective stress σ' as

$$\partial_j \sigma'_{ij} - \partial_i p_f + \rho_m g_i = 0, \tag{1}$$

with all symbols defined in Table 2. We assume an elasto-visco-plastic model. Isotropic linear elasticity is described by Young modulus and Poisson ratio ; plasticity is modelled with an overstress visco-plastic formulation using a flow law of the type $\dot{\epsilon} = \dot{\epsilon}_0 (\Delta\sigma)^m e^{-Ar_m \frac{T_0}{T}}$, where $\Delta\sigma$ represents the overstress. This model presents a rate-hardening effect and in opposite a temperature softening. We use a J2 yield envelope to respect the fact that the existing fault has already pulverised grains and shears without volume change.

The mass balance equation for a fully saturated rock modelled as a solid(s)-fluid(f) mixture, using Darcy's law, can be expressed as
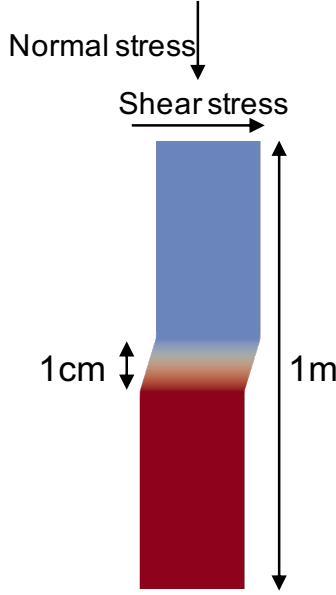
Figure 2: Geometry and stress boundary conditions of the fault at the meso-scale, with constant pore pressure and temperature at both extremities. Fault transverse size is cropped for visualisation purposes.

$$\beta_m \partial_t p_f - \lambda_m \partial_t T + v_i^\beta \partial_i p_f - v_i^\lambda \partial_i T - \partial_i \left(\frac{k}{\mu_f} \left(\partial_i p_f - \rho_f g_i \right) \right) + \partial_i (v_i^{(s)}) = \left(\frac{1}{\rho_f} - \frac{1}{\rho_s} \right) \omega_+ M_B \quad (2)$$

with $v_i^\beta = \left[(1-\phi)\beta_s v_i^{(s)} + \phi\beta_f v_i^{(f)} \right]$ and $v_i^\lambda = \left[(1-\phi)\lambda_s v_i^{(s)} + \phi\lambda_f v_i^{(f)} \right]$. Equation 2 uses a simplified Equation of State of the form $\frac{d\rho_{(i)}}{\rho_{(k)}} = \beta_{(k)} dp_f - \lambda_{(k)} dT, \quad k \in \{s, f\}$. This mass balance equation accounts for the Thermo-Hydro-Mechanical-Chemical processes modelled through the compressibility, thermal expansion, volumetric strain and chemical flux between solid and fluid phases. The permeability k is assumed to evolve, following the common Kozeny-Carman law as a function of porosity $\frac{k}{k_0} = \frac{\phi^3}{\phi_0^3} \frac{(1-\phi_0)^2}{(1-\phi)^2}$.

The energy balance equation provides the temperature evolution within the fault

$$(\rho C_p)_m (\partial_t T + v_i^{(m)} \partial_i T) = \nabla (\alpha \nabla T) + \chi \sigma_{ij} . \dot{\epsilon}_{ij}^p - (E_+ - E_-)(\omega_+ - \omega_-) \quad (3)$$

with χ the Taylor-Quinney coefficient. $V_i^{(k)}$ represents the velocity for the phase $k \in \{s, f\}$. This equation shows that the temperature of the fault can increase due to mechanical dissipation (shear heating) and is balanced by the diffusion term and the energy sink coming from the endothermic chemical reaction considered.

The reaction rates, forward (ω_+) and reverse (ω_-) can be determined at the micro-scale, the physical scale of chemistry, since reactions are taking place at the interface rock-fluid. The active reaction present in a carbonate fault is $CaCO_{3(s)} \rightleftharpoons CO_{2(f)} + CaO_{(s/f)}$. The calcium oxyde being unstable, we consider that half of it ends up being dissolved through reactions that go beyond the scope of this study. With the additional assumption of homogeneous chemical properties at the micro-scale, the chemical reaction can be homogenized to a more generic framework of endothermic chemical dissolutions expressed as $AB_{(solid)} \rightleftharpoons A_{(solid)} + B_{(fluid)}$. This reaction is characterised by its energetics properties (activation energy E, Arrhenius number Ar_c) as well as its kinetics ones (forward and reverse reaction rates and pre-exponential factors A). The advancement of the chemical reaction is described implicitly through its temperature and pressure evolution. Specifically, ω_+ and ω_- are defined as

$$\omega_+ = A_+ (1-s)(1-\phi)\frac{\rho_{AB}}{M_{AB}} e^{-E_+/RT}, \quad (4a)$$

$$\omega_- = A_- s(1-\phi)\Delta\phi_{chem} \frac{\rho_A \rho_B}{\rho_{AB}} \frac{M_{AB}}{M_A M_B} e^{-E_-/RT}. \quad (4b)$$
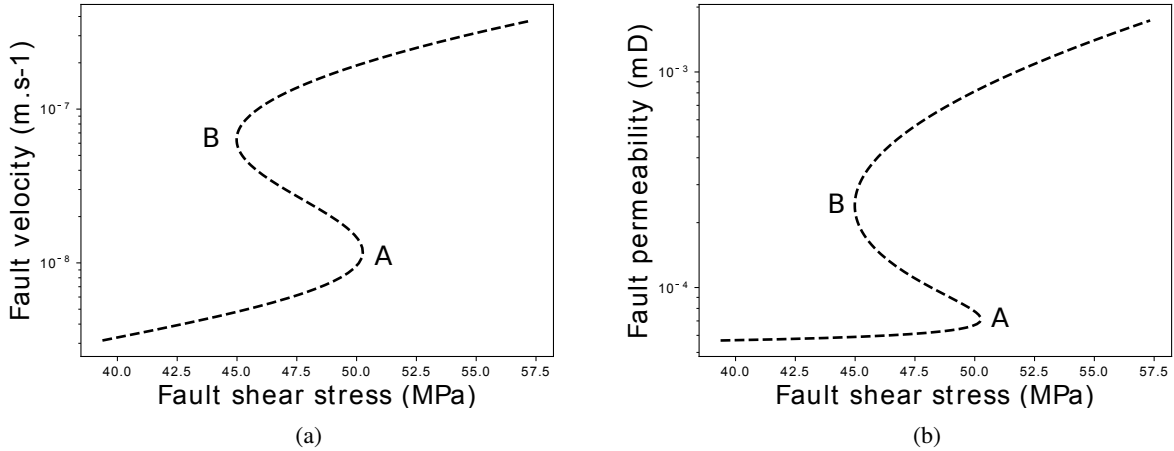
Figure 3: Stability curves of the system using shear stress as the continuation parameter.

The possibility of upscaling directly the chemistry from the micro-scale, in case of more complex or heterogeneous chemical reactions, will be discussed in Sec. 5.

This multiphysics system of equations highlights the complexity of the various feedback processes involved, which are solved in dimensionless form for the displacement, temperature and pore pressure, using the finite element simulator REDBACK (Poulet, Paesold and Veveakis, 2017). Even though the problem is 1D, the system is solved in 2D with periodic boundary conditions, in order to access both components of the stress. While we are interested only in the behaviour of the plastic fault core, heat still dissipates further than the fault core in the elastic region. We therefore model a larger cross section, see Fig. 2, up to where shear heating gets dissipated and far field boundary conditions of temperature can be applied. Moreover, this distance was shown to be the physical length scale of the shear zone system by Poulet et al. (2017), which makes this scale in a sense the master-scale of the system. By capturing the physics at this scale only, Alevizos et al. (2014) have indeed been able to match real case studies of episodic tremors for example.

2.2. Steady-state behaviour of the system

The first step to understand the behaviour of the model is to investigate its stability regimes with respect to some parameters of interest by solving the system of equations in steady-state. The sensitivity analysis is performed using a numerical bifurcation analysis in REDBACK (Tung, Poulet, Alevizos, Veveakis and Regenauer-Lieb, 2017) based on a pseudo-arclength continuation method from Keller (1977). It can provide a continuous evolution of the mathematical solution of the steady-state system with respect to a given parameter, including unstable solutions. This approach is particularly well adapted to track the influence of parameters leading to instabilities such as fault reactivation as can be seen in the original study of the chemical shear zone problem (Alevizos et al., 2014). For the problem of fault reactivation described in Section 7.1, the critical parameter controlling the fault movement at the meso-scale is the shear stress of the fault, which is evolving at the reservoir scale during production. We select therefore the shear stress boundary condition as continuation parameter to study its influence on the fault stability at the meso-scale.

Fig. 3a and 3b show respectively the evolution of slip rate and permeability of the fault and both illustrate the same behaviour. Both figures display a characteristic "S-curve" response of the system explained in details in Alevizos et al. (2014), with three distinct branches. The main driver of the system is the temperature evolution, governed by the thermo-mechanical coupling between shear heating and thermal weakening of the flow law, quantified by the Arrhenius number Ar_m. The lower branch, displayed in solid line on Fig. 3, corresponds to the creeping regime in which the fault is slipping at low velocity ($< 10^{-8} m.s^{-1}$) over the whole range of shear stresses. It represents the case where the fault is shearing slowly enough for the corresponding frictional heat produced to be diffused, keeping the system in the slow creep regime. The thermally activated chemical decomposition is therefore proceeding slowly and the permeability of the fault remains nearly constant, at a low value. The second branch forming the S, displayed in dashed line, is the unstable part of the curve (see Alevizos et al., 2014) and represents a separatrix between the stable lower and upper branches for the range of shear stress values (between 45 and 50 MPa approximatively) where three possible solutions
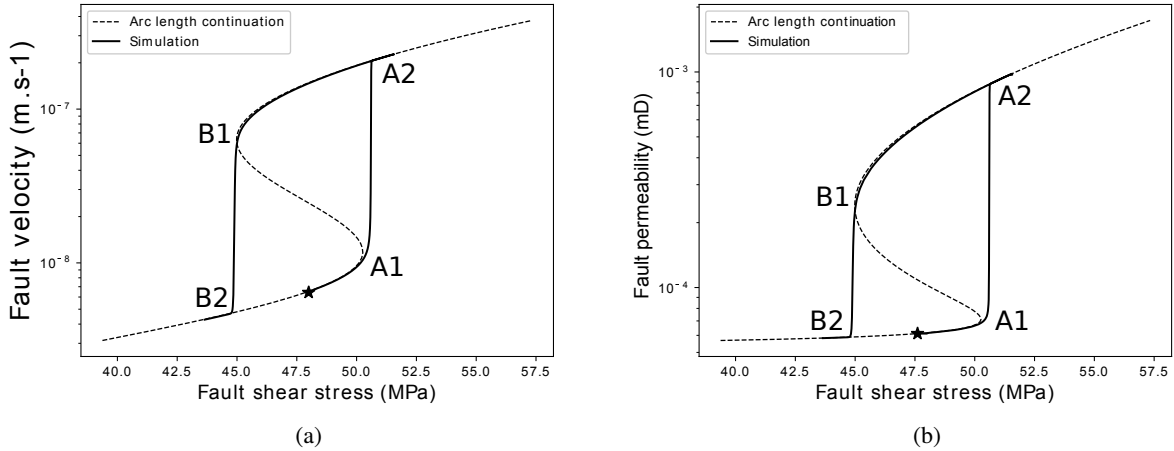
Figure 4: Transient behaviour of the system for an arbitrary loading and unloading. Results are compared with the continuation of Fig. 3. The star represents the start of the simulation.

exist. The higher branch corresponds to the reactivated fault, creeping at much faster rate and characterised by a much higher permeability as the chemical decomposition is fully active. This branch corresponds to the case where the heat generated excesses its diffusion rate and triggers the chemical decomposition reaction

Having established the stability regimes of the system, we now run a transient simulation simulating an induced chemical fault reactivation then deactivation, starting at an initial shear stress value of 47.6 MPa corresponding to the geological conditions of a carbonate fault near criticality at 4km depth, dipping at 60° (scenario from Sec. 7). The shear stress is then arbitrarily moved in two successive phases detailed below. Fig. 4 superposes the results of this transient simulation on top of the steady-state continuation curve displayed on Fig. 3.

During a first phase, the shear stress is increased up to a value of 51.5 MPa to reproduce the scenario of nearby well production. The results show on Fig. 4 that the velocity is initially increasing continuously with shear stress from the initial state (marked with a star) to the first turning point of the stability curve (point A1). This increase of slip velocity is augmenting progressively, along with temperature, due to the thermo-mechanical coupling between shear heating and thermal weakening of the flow law, quantified by the Arrhenius number Ar_m. Bratu (1914) showed that this behaviour is unstable, leading to a thermal runaway. Passed a critical value of shear stress, 50 MPa (point A1), the fault then reactivates as the slip velocity jumps by more than two orders of magnitude, reaching the upper branch at point A2. The capping of the thermal runaway is due to the endothermic nature of the chemical reaction (Veveakis, Alevizos and Vardoulakis, 2010), which stops the temperature instability and keeps the fault in a stable, activated state. The fault activation event is marked simultaneously by a corresponding jump in permeability (see Fig. 4b) as the temperature activated chemical decomposition is actively producing fluid. Further increase of the shear stress moves the system along the upper branch of the S-curve, keeping the velocity and permeability of the fault to high values and augmenting with shear stress (up to the arbitrary end value of 51.5 Mpa).

During a second phase we simulate a stress drop that the fault would experience after activation due to its resulting increased slippage. The stress is decreased from the end value of the first phase, 51.5 MPa, to an arbitrary end value of 43.6 MPa. During the first phase of this stress decrease, we can see that the fault stays activated, as the corresponding steady-state tracing the segment of the upper branch of Fig. 4 between the points A2 and B1. The stress decrease leads indeed to progressive reduction in velocity and permeability through the thermo-mechanical coupling. This process continues until a critical value of stress is reached, 45 MPa, at which point (B1 on Fig. 4) the amount of energy input into the system through shear heating fails to balance the energy dissipated through heat diffusion and the endothermic chemical dissolution. The response of the fault is to drop from point B1 to B2, on the stable lower branch characteristic of the creeping regime with a low velocity. This drop is accompanied by a return of the chemical state close to its original equilibrium through the reverse precipitation reaction which brings back the permeability to a low value. Passed this event, any further evolution of the shear stress moves the fault along the lower branch as explained in the previous paragraph.

2.3. Rate dependency of the system

This stability analysis conducted in the previous section is critical as a preliminary step to determine the key parameters of our system. It provides for example the existence and location of the critical points A and B (see Fig. 3) as well as the velocity of the fault after activation. It can also determine the permeability of the fault after dissolution when the fault has reactivated which is necessary to characterise the leakage of the reservoir after the loss of fault seal.

This steady-state analysis, however, does not account for the dynamics of the system and it is therefore necessary to solve the transient problem to check whether the short production time, compared to the geological time-scale, affects the general behaviour that can be understood from Fig. 3. One could indeed expect some discrepancies due to the transition time required for variables like temperature to switch from one branch to the other. Another interesting aspect to investigate is the rate dependency of the system since the loading rate on the fault depends on the production flow rate applied at the well, which varies during oil and gas operations depending on the production strategy targeted. In this regard, Fig. 5 presents two additional transient simulation results based on the same activation/deactivation scenario shown in Fig. 4 but with slower and faster loading rates. As expected, the response of the system depends on the flow rate and the three resulting curves of Fig. 5 do not superpose, with a difference mostly visible during the unstable path from point B1 to B2 (drop from the higher to the lower branch), and to a lesser extent from point A1 to A2 (jump to from the lower to the higher branch). This difference is easily explained by the fact that the rate dependency is more pronounced during those two transitions, which are quasi-instantaneous. Naturally, a faster loading rate will displace point A2 further along the stress axis and a faster unloading rate will move point B2 to a lower stress value on the lower branch.

It is interesting to note that all results of the transient configurations tested still superpose mostly to the original S-curve. This means that the system remains very close to steady-state when moving along the lower or upper branch and it highlights the critical importance of a steady-state analysis to understand the overall response of a transient scenario. The behaviour of such a chemical fault is mostly driven by the coupled physics of all processes involved and transient phenomena only affect the results at the second order.

This section focused on explaining the physical model used for characterising the ductile behaviour of chemically active faults in high P,T environments. The final results obtained in this section show that the transient behaviour of the fault in Fig. 4 can be for the most critical parts approximated by the steady state behaviour of Fig. 3. Interestingly this figure is directly derived from the combination of the physical mechanisms implemented in Eq. 3, 2, 1. In summary the fault behaviour at such temperatures can be explained predominantly by the physics of the processes involved, contrary to shallower brittle fault where geometry and material heterogeneity control the behaviour of brittle failures. This allows our model to be more predictive towards the detection of fault reactivation and this study showcases the importance of monitoring for example the temperature of deep faults as it is the main tracer of the thermal runaway responsible of the fault activation, discussed in Sec. 2.2.

3. Accounting for the reservoir scale (macro)

While the meso-scale model presented in Sec. 2.1 captures accurately the behaviour of a fault during a reactivation event, the evolution of the principal slip zone and fault core cannot be de-correlated completely from the larger scale. Far field stresses and fluid pressure perturbations can indeed have major impacts on faults, with studies reporting that injection wells could reactivate faults as distant as 90 km apart (Peterie, Miller, Intfen and Gonzales, 2018), with a more accepted average impact distance around 10 km. Without neglecting the importance of other scenarios where faults can be reactivated by drilling directly into them, in this contribution we focus on that less intuitive case of distant reactivation.

The steady-state analysis of the fault at the meso-scale (Alevizos et al., 2014) shows that it is possible to observe episodic stick-slip movements under specific circumstances. Such cases, however, are usually restricted to extreme tectonic environments like subduction zones (Veveakis et al., 2014) or megathrusts (Poulet et al., 2014b). For all other cases, the model of Sec. 2.1 leads to constant creep steady-state, whether slow – locked faults at engineering time-scales – or fast. Under those conditions, a fault reactivation can only be triggered by a change in boundary conditions, which can be accounted for by the modelling of the larger scale. This section describes the macro-scale model selected to simulate a fluid pressure perturbation, including its effect on the fault through pore pressure and stress changes (Sec. 4.1) as well as the feedbacks of the fault evolution on the larger scale (Sec. 4.2).
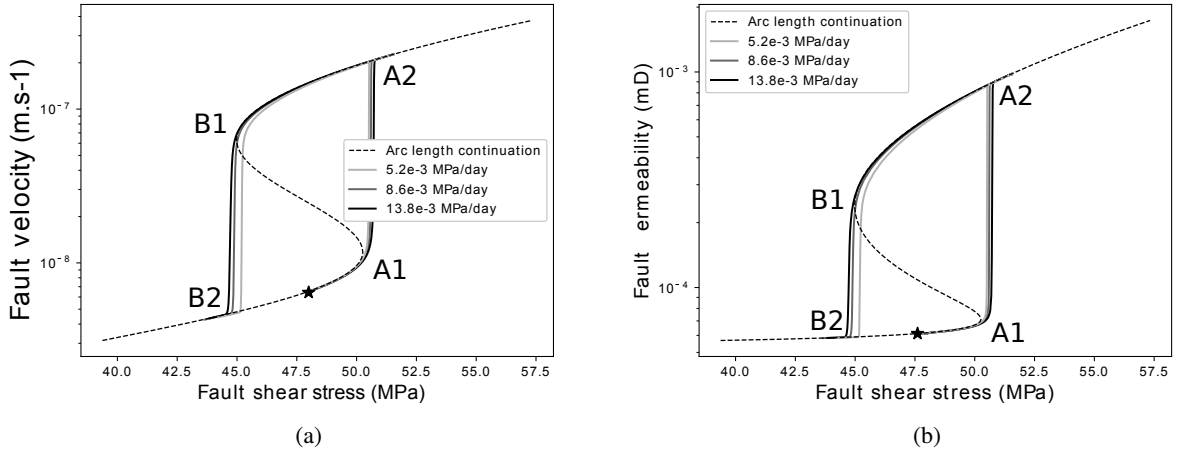
Figure 5: Transient behaviour of the system for an arbitrary loading and unloading. The different curves correspond to different loading/unloading rates and the curves are superposed with the stability analysis of the system. The star represents the start of the simulation.
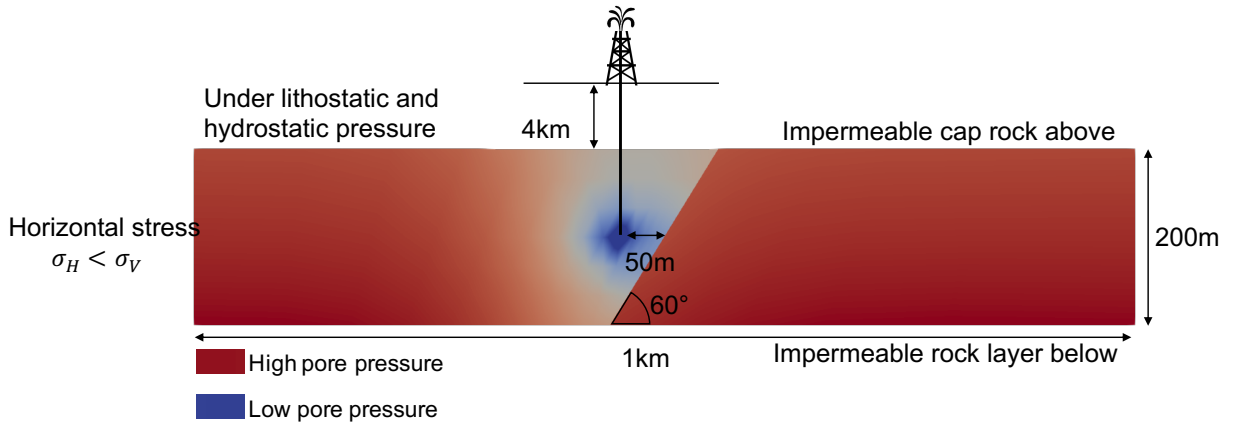
Figure 6: Schematic of macro-scale model showing geometry and boundary conditions.

3.1. Macro-scale environment

For the sake of simplicity, we consider a generic 1 km wide model of a fully saturated fluid reservoir, as shown in Fig. 6, separated in two distinct compartments by an impermeable dipping fault. Various scenarios could be distinguished based on the possible applications to the fields of nuclear waste storage, carbon capture and storage, groundwater extraction, or oil and gas production, but we keep a non-specific scenario to illustrate the more general approach. A fluid perturbation is induced at a source point, located 50m from the fault, and can affect the fault stability through the three physical processes considered: pore fluid pressure, stresses and temperature.

Fluid pressure p and (Cauchy) stress σ_{ij} are linked through the classical poromechanical concept of effective stress (Terzaghi, 1923) $\sigma'_{ij} = \sigma_{ij} - p\delta_{ij}$. A fluid overpressure reaching the fault through diffusion can then classically trigger a fault reactivation through the resulting drop of effective stress (Segall, 1989). This scenario is conveniently illustrated by the Mohr circle, shifted by the pore pressure change and eventually touching a pressure-dependent yield surface.

The fault, with a thickness of the order of metres or less, can't be discretised accurately enough at the kilometre-scale. It is therefore represented by a zero-thickness interface and its behaviour is described using interface laws to link all variables on both sides, as presented in the next section.

The reservoir at the macro-scale is mainly influenced by the fluid's movement and resulting mechanical deformation

through the poromechanical couplings. The fluid motion at this scale is largely governed by the permeability and the flow obeys Darcy's law. Note that for the sole purpose of showcasing the framework in this contribution, we focus on the application example of fluid production, see Sec. 7. In addition, the shear heating of the fault has no neighbouring influence at the scale of the reservoir. For these reasons, we consider for the macro-scale model that the temperature in the reservoir remains constant and do not model its evolution. Overall, the large scale model is well characterised by the momentum and mass balance equations, including gravity, written as

$$\partial_j \sigma'_{ij} - \partial_i p + \rho_m g_i = 0, \tag{5}$$

$$\partial_t p - \partial_i \left[\frac{k}{\mu_f} (\partial_i p - \rho_f g_i) \right] = 0, \tag{6}$$

where ρ_m is the density of the solid-fluid mixture. Even though the fault undergoes some important plastic strain, plasticity usually remains restricted to the principal slip zone and surrounding fault core. We consider therefore the reservoir to deform elastically even when the fault slips. Without loss of generality, we select an isotropic linear elastic constitutive model characterised by the Young's modulus E and the Poisson ratio ν.

3.2. Interface laws for the fault

The negligible thickness of the fault compared to the length scale of the reservoir justifies the choice of modelling the fault as an interface, rather than facing the prohibitive computational costs associated with the discretisation of that feature at the large scale. The fault is then modelled at the meso-scale and considered at steady state at each timestep at the macro-scale, with its impact accounted for at that level through interface laws implemented in REDBACK for the mechanics and fluid flow, allowing us to solve hydro-mechanical simulations with discontinuous fields of pore pressure and displacement.

We take advantage of the support for interfaces in the MOOSE framework, which handles automatically the duplication of nodes at interfaces and allows the handling of discontinuous variables simply through the implementation of the weak form terms needed at the interface.

3.2.1. Hydraulic

The flow behaviour at the fault interface, described by its normal vector $n_i^{(F)}$, is a critical feature for the macro-scale simulation. Faults can indeed form impermeable barriers between reservoir compartments, which have been known to transform temporarily into fluid pathways during fault reactivations, as reported in the cases of Wiprut and Zoback (2000) and Dos Santos and Oliveira (2014). To model this behaviour, the interface is assigned an effective thickness H_F and permeability $k^{(F)}$ so the difference of pore pressure between the two sides of the interface (F), denoted by the exponents (A) and (B), can be computed using Darcy's flow. Assuming fluid incompressibility, the continuity of flux can be written as

$$\frac{k^{(R)}}{\mu_f} (\partial_i p^{(R)} - \rho_f g_i) n_i^{(F)} = \frac{k^{(F)}}{\mu_f} (\partial_i p^{(F)} - \rho_f g_i) n_i^{(F)}, \tag{7}$$

where the exponent (F) and (R) refer to the fault (interface) and reservoir respectively. The gradient of pressure across the interface is computed as

$$\partial_i p^{(F)} n_i^{(F)} = \frac{\Delta p}{H_F} = \frac{p^{(A)} - p^{(B)}}{H_F}. \tag{8}$$

Combining 8 and 7 we end up with an equation for the interface law defined for each pressure variable as:

$$-\frac{k^{(A)}}{\mu_f} p_{,i}^{(A)} n_i^{(F)} + \frac{k^{(F)}}{\mu_f} \frac{p^{(B)} - p^{(A)}}{H_F} + \frac{\rho_f g_i n_i^{(F)}}{\mu_f} (k^{(A)} - k^{(F)}) = 0 \tag{9}$$

$$-\frac{k^{(B)}}{\mu_f} p_{,i}^{(B)} n_i^{(F)} + \frac{k^{(F)}}{\mu_f} \frac{p^{(B)} - p^{(A)}}{H_F} + \frac{\rho_f g_i n_i^{(F)}}{\mu_f} (k^{(B)} - k^{(F)}) = 0 \tag{10}$$

To verify the implementation of this pore pressure interface, we compare the results against an analytical problem for a simple one-dimensional (1D) case. We consider three regions (R_1, R_2, R_3) of various thicknesses (D_1, D_2, D_3)
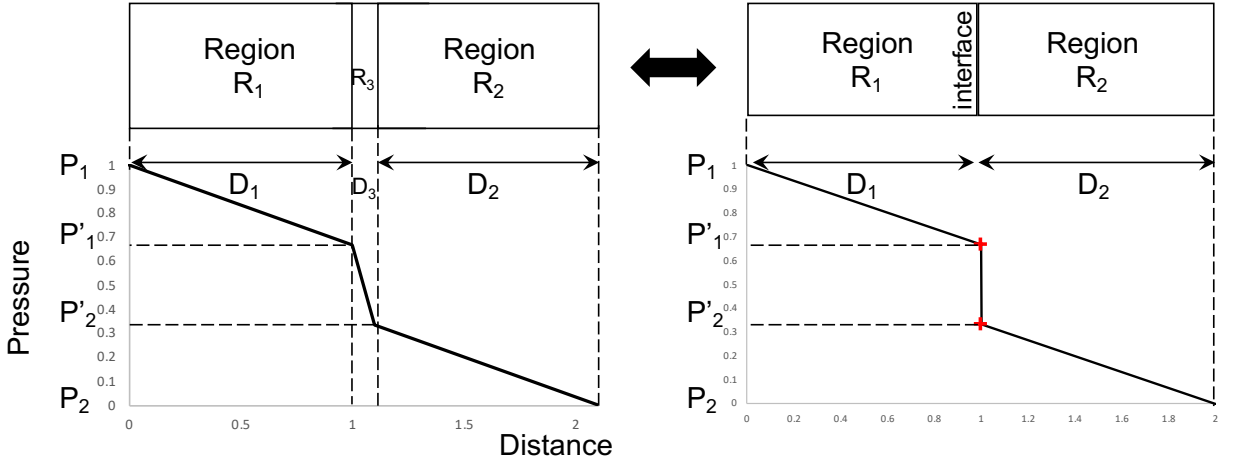
Figure 7: Model used to benchmark the flow interface. The specific case plotted is described by $D1 = D2 = 10 \times D3$; $p_1 = 1$ and $p_2 = 0$; $k_1 = k_2 = 10 \times k_3$. On the left are plotted the result for the system fully resolved and on the right for the reduced system with interface. The system with interface matches with machine precision the results of the full system, highlighted with the red crosses.

and permeability values (k_1, k_2, k_3), as shown in Fig. 7 and solve for the steady-state of the 1D horizontal flow through. We apply a pressure gradient across these three blocks with constant boundary conditions at each end (p_1 and p_2). The two pressures p'_1 and p'_2 at the interface between the regions 1-3 and 2-3 can be expressed as:

$$p'_2 = \frac{k_1 k_3 D_2 D_3 p_1 + k_2 D_3 (k_1 D_3 + k_3 D_1) p_3}{(k_3 D_2 + k_2 D_3) * (k_1 D_3 + k_3 D_1) - k_3 k_3 D_1 D_2}, \tag{11}$$

$$p'_1 = \frac{k_1 D_3 p_1 + k_3 D_1 p'_2}{k_1 D_3 + k_3 D_1}. \tag{12}$$

This analytical solution is used to validate the numerical results obtained by solving a similar problem where the middle region is replaced by a flat interface, on Fig. 7.

3.2.2. Mechanical

The mechanical behaviour of the fault can also be accounted for at the macro-scale with an interface, to accommodate the displacement generated by a slip event modelled with an arbitrary friction law or in the case of this contribution with the dynamic upscaling of the meso-scale model. Given the negligible thickness of the fault at the large scale, the problem reduces to a sliding block problem and we use the same environment as described above for the flow. We introduce the two displacement fields $u_i^{(A)}$ and $u_i^{(B)}$ on both sides of the fault, marking the discontinuity at the interface.

For a sliding block problem, common interface approaches include frictional laws such as rate-and-state laws. Interestingly, the model presented in Section 2.1 presents a generalisation of the rate-and-state friction law through a physical approach which identifies the role of temperature and pore pressure in the evolution of the effective friction coefficient (Veveakis, Alevizos and Poulet, 2017). This model offers therefore a more general tool in the specific context of chemical shear zones, extending the knowledge from the more empirical approaches. To integrate that model in our multiscale framework we introduce a mechanical interface law which takes for input a displacement jump between each side of the interface and that is compatible with the value of the stresses applied to the fault through the constitutive model assumed.

The displacement jump $\Delta u_i^{(F)}$ follows the equation:

$$u_i^{(A)} - u_i^{(B)} + \Delta u_i^{(F)} = 0 \tag{13}$$

It can be noted that the displacement discontinuity across the shear zone is negligible since most of the deformations happen in shear and the shear zone itself has a negligible size at the macro-scale. It means that the displacements are
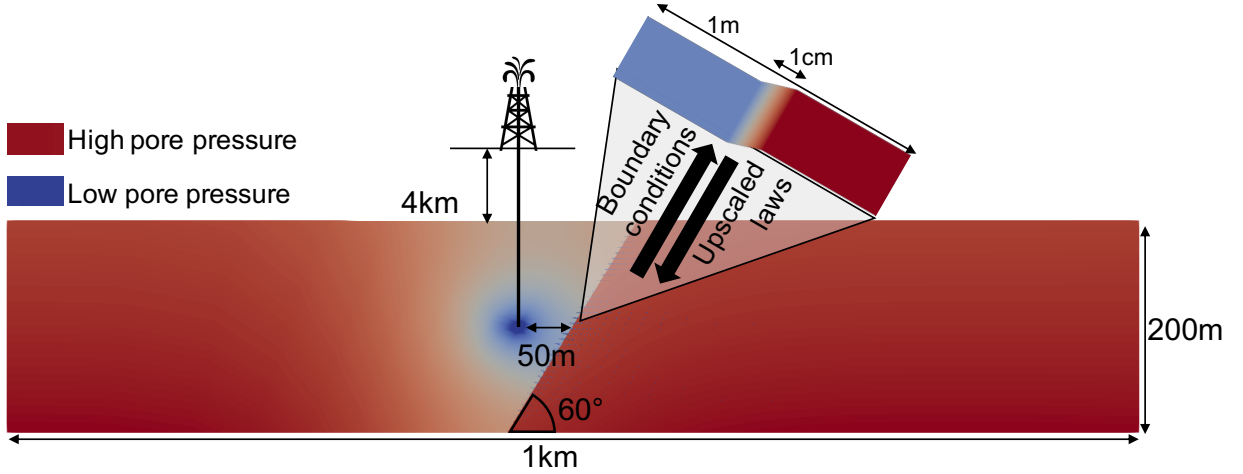
Figure 8: Two-way couplings for the macro/meso-scale model.

discontinuous only tangentially to the fault and it simplifies Eq. 13 to

$$u_i^{(A)} - u_i^{(B)} + \Delta u^{(F)} w_i^{(F)} = 0 \tag{14}$$

with $w_i^{(F)}$ the tangent unit vector of the fault.

In addition to this constraint on the displacement, the mechanical law for the interface needs to respect the stress equilibrium. This condition translates to the continuity of the traction across the interface and this relationship is written as:

$$(\sigma_{ij}^{(A)\prime} + p^{(A)} \delta_{ij}) n_i^{(F)} = (\sigma_{ij}^{(B)\prime} + p^{(B)} \delta_{ij}) n_i^{(F)} \tag{15}$$

Note that the total stress is continuous despite the fluid pressure discontinuity at the interface (see Sec. 3.2.1), making the effective stress discontinuous as well.

The two conditions (Eq. 13 and 15) are enforced weakly using a penalty method. Eq. 13 is used to define the error $\delta u_i = u_i^{(A)} - u_i^{(B)} - \Delta u_i^{(F)}$, which can be interpreted physically by considering a virtual spring at the interface with a high spring constant α, that we take as the penalty parameter. Following this approach, the traction on each side of the interface is equal to the product of α times the elongation δu_i of the spring, which enforces continuity of the traction across the interface. Numerically, the higher the value of α, the smaller the error δu_i on our displacement discontinuity condition. In this contribution, the value of 10^6 proved to be sufficient.

4. Macro/meso-scale couplings

In order to have a model that can study real phenomena of fault reactivation and their consequences, the connection of the macro-scale to the meso-scale is necessary. Indeed, as stated before, the meso-scale cannot simulate a realistic scenario of fault reactivation because the perturbation that cause it happens at a larger scale. On the other hand, the macro-scale model alone is also insufficient: it lacks a physical law for the interface that links the stress experienced by the fault to both the slippage and the evolution of permeability.

These holes can be filled by considering a macro/meso-scale model that couples both the scales. In this multiscale model, the perturbation simulated at the macro-scale is transferred to the interface and applied as a boundary condition for the meso-scale. The meso-scale is now solving for a dynamic boundary value problem that can actually place the fault reactivation in its context. The macro-scale can in turn obtain the missing constitutive law for the interface by upscaling directly the behaviour of the fault from the meso-scale. These couplings are summarised in Fig. 8.

In order to have the interface fully characterised, common multiscale models would select directly all the nodes on the interface to perform an upscaling. However, in order to reduce on computational costs, we choose to select only certain points of interest along the interface and interpolate the upscaled properties in between.

4.1. Transfer of boundary conditions

The macro scale provides the dynamic boundary conditions for the meso-scale. These boundary conditions are the normal and tangential stress to the fault, the two pore pressures and the temperature that are applied to the fault at the macro-scale.

For simplicity, we consider the fault at the meso-scale in its local referential as seen in Fig. 8 (where the fault is horizontal). Since the fault is cutting the reservoir with a dip angle of θ, see Fig. 6, the two referential are rotated from one another by θ. It means that we need to transfer from the macro-scale the normal and tangential stress in the local referential of the fault. The formula is derived by decomposing the traction vector at the fault $t_i = \sigma_{ij} n_j$ into his normal (N) and tangential (T) component in the local referential of the fault.

$$t_i = t_i^{(N)} + t_i^{(T)} = \sigma_{ij} n_j \tag{16}$$

$$t_i^{(N)} = (t_j n_j) n_i = ((\sigma_{jk} n_k) n_j) n_i \tag{17}$$

$$t_i^{(T)} = t_i - t_i^{(N)} = \sigma_{ij} n_j - ((\sigma_{jk} n_k) n_j) n_i \tag{18}$$

As seen in Eq. 17-18, the formulas make use of the normal vector n_i. Since n_i is computed for each element separately in the finite element simulator. We do not need to assume a linear fault dipping at a given angle θ, the interface can be a curve with a normal vector n_i defined at each discretised segment.

4.2. Feedbacks to the interface law

Displacement discontinuity The mechanical interface law takes in input the stress applied to the fault and returns the displacement discontinuity tangential to the fault. Contrary to most interface laws, it does not assume any constitutive law to solve for this discontinuity. Instead it upscales a physical law from the meso-scale.

With the set of boundary conditions provided from the macro-scale, the chemical shear zone model can solve for the displacement across the shear zone. The difference of displacement between each side of the shear zone is the discontinuity of displacement that is transferred to the macro-scale and applied at the interface's corresponding material point using Eq. 14.

Permeability evolution The macro-scale needs to capture the evolution of permeability, being solved at the meso-scale, in order to simulate the pressure equilibration that happens after reactivation of the fault. For this reason, the permeability of the fault computed at the meso-scale is transferred and applied on the fault at the macro-scale. The upscaling of this permeability is not straightforward. The reason is that when reactivation occurs, a part of the fault dissolves. The permeability is therefore not homogeneous across the fault at the meso-scale. The homogenisation we want to perform has to respect the condition that the averaged darcy flow across the fault at the meso-scale is equal to the flow inputted in the interface law of Sec. 3.2.1. This condition translates to:

$$\frac{k^{(F)}}{\mu_f} \frac{p^{(B)} - p^{(A)}}{H_F} = \frac{1}{H_F} \int_A^B \frac{k^{(M)}}{\mu_f} \partial_i p^{(M)} n_i^{(F)} \tag{19}$$

where (M) design the meso-scale values. With Eq. 19, we can express the homogenised value of permeability for the fault as:

$$k^{(F)} = \frac{1}{p^{(B)} - p^{(A)}} \int_A^B k^{(M)} \partial_i p^{(M)} n_i^{(F)} \tag{20}$$

5. Enriching the meso-scale model from a lower scale (micro)

On top of all efforts to homogenise micro-processes at the meso-scale (see Sec. 2), direct modelling of specific phenomena at the micro-scale can add a level of refinement that cannot be accounted for by static homogenisation. In this contribution the lower scale of interest is the one at the micrometre level where the microstructure can be discretised as pore space and solid matrix. At this scale, the complex evolution of the pore microstructure results from the interplay between geometry and the major non-linear feedbacks linking all physical processes involved, mechanical, thermal, hydraulic, chemical. In turn the evolution of this microstructure affects the upper scale in terms of homogenisation of material properties and constitutive relationships. Selecting the list of properties to upscale is a balancing act between

accuracy and computational cost. As mentioned in Sec. 2, capturing the essence of a micro-scale process at the meso-scale also presents huge benefits for the stability analysis, which can then quantitatively account for. As such, even though many phenomena are rooted at the micro-scale, only a limited number of critical ones will usually be upscaled numerically for each of the THMC physic.

For the flow, upscaling of permeability has been an active area of research since the discovery of using µCT-scanning for rocks (Blunt, Bijeljic, Dong, Gharbi, Iglauer, Mostaghimi, Paluszny and Pentland, 2013). The relationship between porosity and permeability for instance, which can even been negatively correlated in some cases (e.g. Morin, 2006), is inherently dependent on the pore or grain structure. It can't always be represented by empirical laws to use directly at the meso-scale and do require specific modelling at the micro-scale to capture the inherent complexity. The other common upscaling is the mechanical behaviour where discretising the grains using Discrete Element Method allows to upscale directly a constitutive mechanical model at the upper scale (Nitka, Combe, Dascalu and Desrues, 2011) and helps resolve regularisation of the mechanical localisation (Desrues, Argilaga, Pont, Combe, Caillerie and kein Nguyen, 2017). The upscaling of thermal processes is usually not done since the temperature is considered constant at the micro-scale. Regarding the chemistry, the upscaling process is tedious as the micro-scale involves the interplay of numerous chemical reactions.

In the context of a fault reactivation in a reservoir, the permeability is the most important parameter as it affects both the onset of reactivation (Alevizos et al., 2014) and the amount of resulting leakage across the fault. When specifically considering a low permeability chemical shear zone, chemical dissolution and precipitation can be responsible for permeability evolution of orders of magnitude (Poulet et al., 2017). In comparison the change of permeability induced by other mechanisms, such as hydromechanical, is negligible. For this reason we will focus in this contribution specifically on the chemical alteration of the rock microstructure.

Chemical reactions at the micro-scale can include many different aspects which remain active fields of research, including fluids mixing, fluid-rock interactions, advection, diffusion, electrochemical migration and all coupled combinations of those processes (see review from Yoon, Kang and Valocchi (2015)). A comprehensive micro-scale chemical simulator falls therefore outside the scope of this thesis and we follow instead an illustrative approach by considering a homogenised model of the chemical reaction considered as presented in Sec. 2. For the application to fault reactivation, the advantages of using an analytical computation of chemical porosity evolution at the meso-scale outweigh largely the drawbacks of not simulating the chemical reactions directly at the micro-scale. The benefits are clear in terms of numerical efficiency (speed and convergence) but also for the resulting ability to run stability analyses (Alevizos et al., 2014) to understand and quantify the impact of all material parameters.

Since the focus of our study is not to present the most accurate model at the micro-scale, but to demonstrate how the effects at that scale can be linked to the next scale up, we restrict ourselves to the simplest case where the dissolution only depends on the microstructure geometry, independently from the distribution of flow velocity, stress or other properties. This choice also fits nicely with the application of fault reactivation selected in this contribution where the flow remains low and host rocks like carbonates can be quite homogeneous. The dissolution can then be decoupled from the flow and both computed sequentially. As explained above, the change of porosity $\Delta\phi_{chem}$ stemming from chemical dissolution/precipitation is computed at the meso-scale (see Sec. 2) and fed to the micro-scale where its spatial distribution is evaluated in order to update the permeability from a flow simulation. The first section focuses on explaining the erosion/dilation algorithm used for accommodating $\Delta\phi_{chem}$ at the micro-scale. The second section compares this algorithm with the Kozeny-Carman law.

Simulations at the micro-scale require a 3D mesh capturing the geometry of the pore space and solid matrix. The finite element mesh represent digital rock samples reconstituted from µCT-scan images. Since raw µCT-scan images display however only a density variation in a continuous grayscale manner, a first pre-processing treatment of the image, called segmentation, is needed in order to differentiate the rock matrix from the pore space. To obtain the final digital rock samples, we use the methodology of Lesueur, Casadiego, Veveakis and Poulet (2017) that developed a framework to construct 3D meshes from a stack of already segmented 2D µCT-scan images.

5.1. Erosion/dilation algorithm

The effective chemical reaction considered in our model is a dissolution of the solid skeleton (see Sec. 2.1), triggered by the rise of temperature of the fault's core due to shear heating. Assuming uniform temperature at the micro-scale and chemical homogeneity of the sample, the dissolution can be considered to happen homogeneously at the surface of the pore space. Given the target change $\Delta\phi_{chem}$ of porosity imposed by the meso-scale, we implemented a geometrical erosion/dilation algorithm which switches the nature of layers of voxels between pore space and solid matrix at the
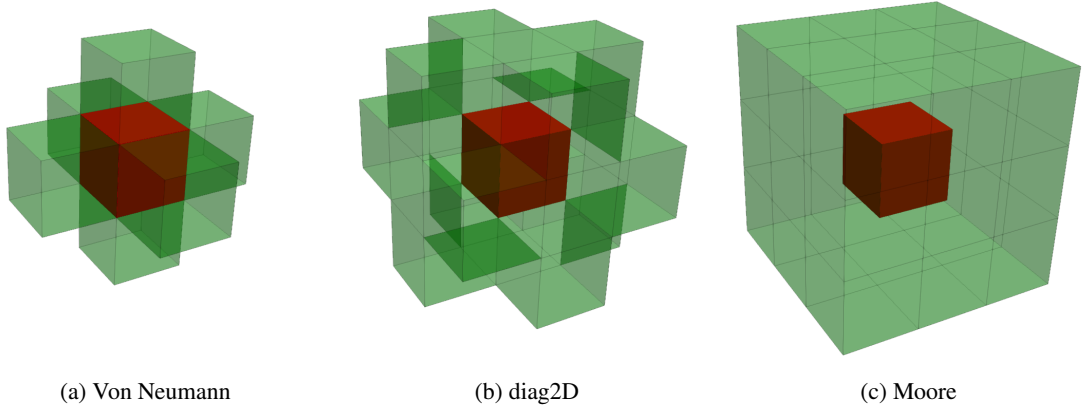
(a) Von Neumann   (b) diag2D   (c) Moore

Figure 9: Visualisation of the three types of neighbourhoods

interface. Since a dilation of the pore space is equivalent to an erosion of the solid space, we only need to describe the erosion algorithm. The target change $\Delta\phi_{chem}$ is converted to a target volume ΔV and the algorithm evaluates successively whether a kth layer of volume V_k should be converted from pore to solid, in order to approach the volume target as closely as possible without exceeding it.

$$\sum_{k=1}^{n} V_k \leqslant \Delta V < \sum_{k=1}^{n+1} V_k \tag{21}$$

Removing a discrete number of layers introduces a numerical discretisation of the porosity evolution, which can be kept monotonous by approaching ΔV with its infimum value (Eq. 21). This approach also captures well the general behaviour of the fault which is creeping slowly during most of the simulation, with barely any change in porosity, and evolving quickly during slip events marked by large porosity changes. The computed porosity remains thereby identical to its initial value until a slip event becomes perceptible, after which the porosity jumps by steps controlled by the mesh resolution. The erosion of each successive layer (of index k) is done by the function $BoundaryElements$ described hereunder.

BoundaryElements This function is used to find all elements at the pore-grain interface and computes the volume of the next layer to be eroded. It parses all mesh elements and queries each $SubdomainID$ to compare it with those of its neighbours. Each element identified as grain ($SubdomainID = 1$) with at least one of its neighbours representing a pore ($SubdomainID = 0$) is added to the list of interface elements, whose $SubdomainID$ is switched from 1 to 0 once the whole mesh is parsed. The corresponding volume V_k is then used to assess the termination of the iterative algorithm (Eq. 21) before the next iteration ($k + 1$) can start if need be.

5.1.1. Elements neighbourhoods

For a regular grid, there exist three types of element neighbourhood. The simpler one considers only the elements sharing a common face with the element queried and this neighbourhood is referred as *von Neumann*. The *diag2D* type considers elements sharing common edges as well, and the *Moore* type considers elements sharing any corner point. These three neighbourhoods are visualised in Fig. 9. In order to select the most appropriate type for our model, we first check the erosion of some of the fundamental shapes that are found in segmented μCT-scans of rocks.

The first shape that we erode is the cube since the mesh of the rock microstructure is a reconstruction of μCT-scans images, that are naturally pixelated. From the initial cube displayed in Fig. 10, we apply a high level of erosion using the three type of neighbourhood presented above. We can see in Fig. 10 that using the von Neumann neighbourhood erodes the cube in a spherical manner, as a small rhombicuboctahedron, whereas with the Moore neighbourhood we retain a perfect cubic shape. With the diag2D neighbourhood we obtain an eroded shape in between the two, a truncated cube. It is important to note that we do not necessarily want to retain the cubic shape of the pixel since the discretisation is a distortion of the real microstructure. In this case the Moore neighbourhood is less attractive.

The second shape that we erode is the sphere since we are mostly dealing with granular materials. Indeed, if the
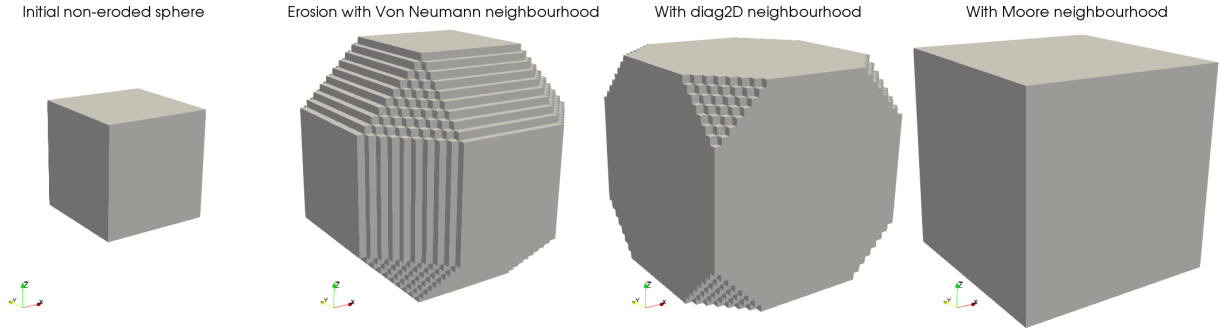
Figure 10: Erosion of a cube by considering three different types of neighbourhood.
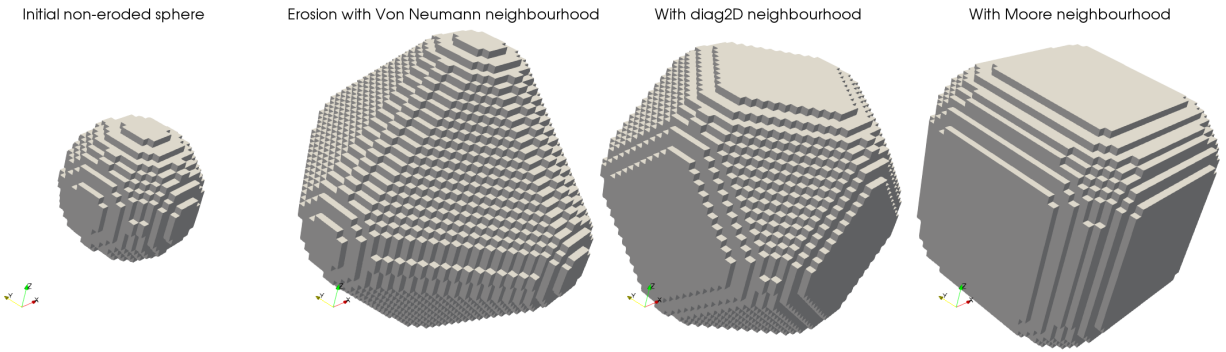
Figure 11: Erosion of a sphere by considering three different types of neighbourhood.

resolution of the μCT-scan is high enough, we should see more or less spherical grains. In this case we can see in Fig. 10 that the von Neumann neighbourhood creates a regular octahedron, which differs a lot from the initial sphere. On the other hand, the Moore neighbourhood will erode the sphere into a cube-like shape. It is the diag2D neighbourhood that approaches a spherical erosion the most. It is more realistic that the erosion retains the spherical shape of the grain which brings us to select the diag2D neighbourhood for the rest of the contribution, in agreement with the study on the cube shape.

Still, we can note from Fig. 12 that the different implementations do not change much the geometry of the microstructure for reasonable levels of dissolution/precipitation.

5.1.2. Mesh resolution sensitivity on porosity evolution

The mesh resolution has obviously a direct impact on the discretisation of the porosity evolution with the erosion level, leading to the usual compromise between precision and computational time. Fig. 13a shows the porosity evolution with the number of eroded layers for two different initial mesh resolutions, highlighting the expected gain in porosity resolution with increased refinement. Given the good resolution of the initial mesh, those porosity curves are particularly smooth and a different behaviour can be expected for the corresponding permeability evolution.

### 5.2. Flow simulator and permeability upscaling

We consider a porous rock at the micro-scale composed of a solid matrix and a pore space containing a single phase incompressible fluid. Given the geological applications targeted, we can restrict the study to the case of low-velocity flow and consider therefore the flow to be laminar. For the purpose of computing permeability, solving the steady-state flow is even sufficient. Based on these assumptions the system is reduced to the traditional Stokes equations. To solve this system of equations on digital rock samples reconstructed from μCT-scan images and upscale the permeability, we use the methodology introduced by Lesueur et al. (2017) with only a slight modification of the system of equations,
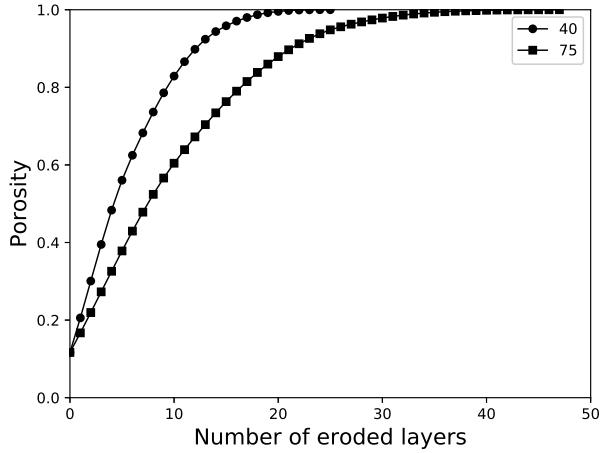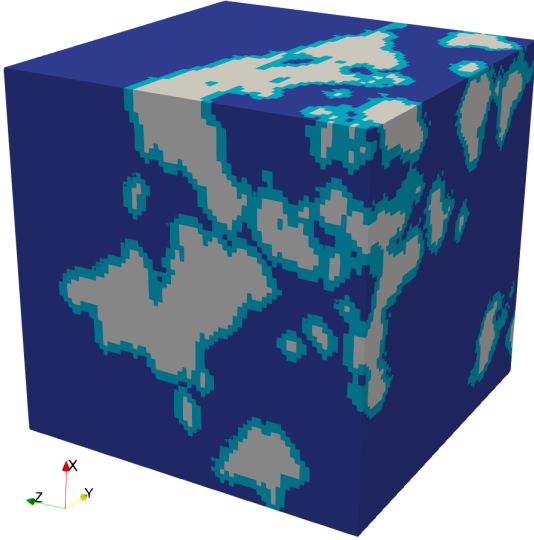
Precipitation of
Von Neumann neighbourhood   diag2D neighbourhood   Moore neighbourhood
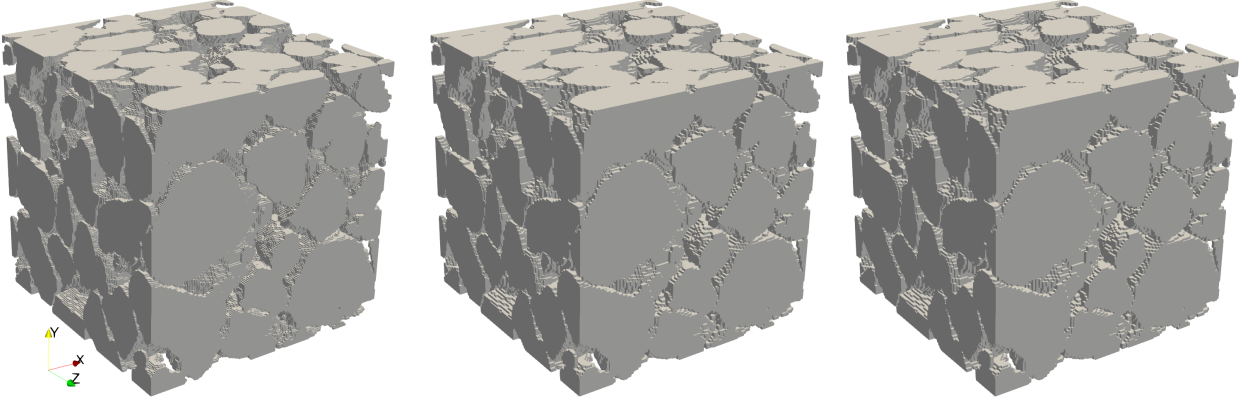
Figure 12: Comparison of the three types of element neighbourhood during the precipitation of a 1.2 mm^3 size sample of the LV60A sand pack from its initial porosity of 37% to a target value of 27%.

(a) Visualisation of a few eroded layers in bright blue. In white is the pore space; In dark blue are the grains.

(b) Evolution of layers volume at different resolutions. The graphs en-titled n have a resolution of $n \times n \times n$.

Figure 13: Study on the error made on $\Delta\phi$ using the erosion algorithm at different resolutions on a 0.2 mm^3 subsample of the carbonate rock C1 from Imperial College Consortium On Pore-Scale Modelling (2014a).

detailed below.

    Imposing no-slip boundary conditions at the pore-grain interface requires the identification and tracking of that interface at every timestep, which can become a numerical challenge by itself when the interface evolves in time due to mechanical deformation or chemical alteration of the microstructure. Fortunately, this issue can be avoided altogether using a slightly different approach and solving for the Darcy-Brinkman system of equations, which was introduced by Brinkman (1949) as an extension of Darcy's law in order to be able to simulate "*the viscous force exerted by a flowing fluid on a dense swarm of particles*" (Brinkman, 1949). It can be expressed in a dimensionless form as

$$-\frac{1}{Re}\nabla^2 \vec{v_f}^* + \frac{1}{Re\,k^*}\vec{v_f}^* + \nabla p_f^* = 0, \tag{22}$$

$$-\nabla \cdot \vec{v}_f^{\,*} = 0, \tag{23}$$

where $k^* = \frac{k}{L_{ref}^2}$ is the normalised permeability. This system is particularly useful to simulate flow in fractured porous media, for instance, as the usage of the permeability in the second term of Eq. 22 allows an easy handling of the flow with Darcy's law in the matrix, where the permeability value is determined, as well as in the fractures, where the permeability would be considered infinite, simply cancelling that term in the equation and reducing the system to Stokes flow. The same approach can be used on a micro-scale structure, using infinite permeability in the pore space (10^{15} in this contribution) and an arbitrary low but positive value of permeability within the solid matrix (10^{-15} in this contribution), as the grains are considered impermeable. This technique allows to simulate the flow within the pore space without having to specify the interface.

5.3. Deviation from Kozeny-Carman law due to precipitation

The algorithm described in this section combined with the flow simulator of Sec. 5.2 allows to study the evolution of permeability during homogeneous dissolution/precipitation for any type of rock microstructure. When used in the multiscale framework, this model is meant to replace empirical laws of permeability evolution by a dynamic physical upscaling. The most commonly used empirical law to estimate permeability from changes in the microstructure is the Kozeny-Carman law, which links permeability to porosity. A multitude of rocks have been calibrated to respect the Kozeny-Carman law (Chapuis and Aubertin, 2003; Heijs and Lowe, 1995) but most studies focus on static porosity (Doyen, 1988) and few have been made on the validity of the law after precipitation, which is what we verify in this section.

The material selected for this study is the LV60A sand pack (Imperial College Consortium On Pore-Scale Modelling, 2014b), which should respect the Kozeny-Carman law particularly well because of its granular structure, due to non-consolidation. The Kozeny-Carman law chosen for this section is the more general form, originally established before making the hypothesis that the media is represented by a packing of spheres. Indeed, although the grains of this natural sand pack are as spherical as can be found in a geomaterial, they are not perfect spheres. This formulation of the law reads as

$$k = \frac{1}{K} \frac{\phi^3}{S^2}, \tag{24}$$

where K represents the Kozeny's constant and S the specific surface area, in m^{-1}, denoting the area of the pore space divided by the bulk volume of the rock sample.

The size of the subsample is taken at 1.2 mm^3, larger than the REV size of permeability which was computed to be $\approx$1 mm^3 by Mostaghimi et al. (2012). The unprecipitated sand pack's permeability was calibrated to match the Kozeny-Carman law for the corresponding initial porosity of 37.6%, as shown on Fig. 14 by the superposition of the points on the far right hand side. This fit was obtained by taking a value of the Kozeny constant $K = 3.915$, which falls close to the value of 5 proposed by Ergun and Orning (1949) for a packed bed of spheres, as predicted, and was kept constant for the rest of the simulation.

The rest of the figure shows the evolution of this sand pack's permeability during precipitation, running through the graph from right to left, with porosity values decreasing from the initial 37.6% to 5%. we observe that the higher the precipitation level, the further the deviation from the Kozeny-Carman law. This can be explained by the fact that precipitation creates thicker bonds at the grains contact which were initially perfect. The porous medium can no longer be assimilated to a packing of spheres and this deviation from the hypothesis of the model justifies the difference in behaviour. As mentioned in Sec. 5.1.1, we note that the porosity-permeability relationship is not affected much by the different types of neighbourhood considered, since all three types of erosion fall approximately on the same interpolated curve in Fig. 14.

5.4. Loss of Representative Elementary Volume (REV) with precipitation

The homogenisation of a property like permeability requires to be working on a REV of the pore structure for this specific property in order for the homogenisation approach to be valid (Hill, 1963; Bear, 1972). Interestingly, a REV for the geometry of the pore structure itself does not infer that the REV is achieved for the property considered. For example, Mostaghimi et al. (2012) showed for multiple digitised rocks that porosity had a much smaller REV than permeability. The determination of the REV size for a given microstructure remains a challenging task and for instance even the existence of the REV for heterogeneous rocks like carbonate remains an open question (Mostaghimi et al.,
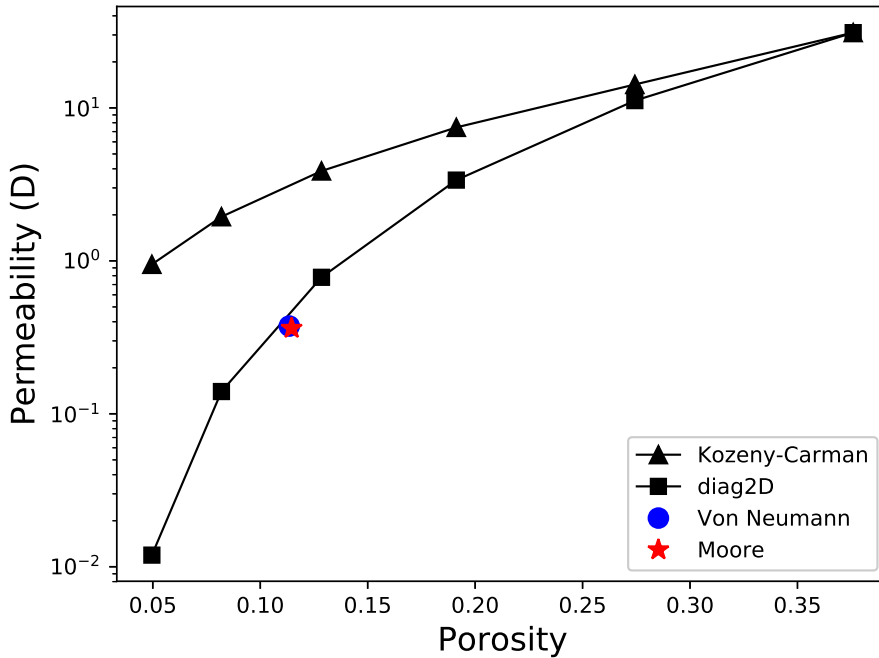
Figure 14: Permeability evolution (solid line with squares) during the precipitation of a 1.2 mm^3 subsample of the LV60A sand pack from an initial 37.6% porosity down to 5%. Superposed is the permeability (solid line with triangles) calculated using the Kozeny-Carman law of Eq. 24, calibrated to the unprecipitated state using $K = 3.915$. In comparison to the diag2D neighbourhood, we plot one advanced state of precipitation of the same sample using separately the Von Neumann (blue circle) and the Moore (red star) neighbourhood.

2012). An extra level of complexity gets added when considering chemical alterations. Dissolution and precipitation mechanisms change indeed the geometry of the microstructure dynamically which in turn affects the REV size.

Indeed, Fig. 15a shows that in addition to losing the grain's spherical shape with precipitation, we are losing the REV convergence of the sample. This is visually highlighted on Fig. 15b where we can see that the very homogeneous flow in the initial sample has been reduced to two major flow paths after precipitation. If the precipitation ends up closing flow channels, the flow has high chances to become heterogeneous and as such, the size of the REV increases.

An REV analysis was performed on that sample by increasing the sample size from 0.6 mm^3 to its full size of 1.2 mm^3 and computing the permeability in each case. Fig. 15a plots the evolution of normalised permeability with the relative sample size and shows that precipitation not only affects the grains' sphericity but the REV convergence altogether. This is visually highlighted on Fig. 15b where we can see that the very homogeneous flow in the initial sample has been reduced to two major flow paths after precipitation. With precipitation closing flow channels, the flow naturally become more heterogeneous and, as such, the size of the REV increases, explaining the non-convergence observed in Fig. 15a.

6. Meso/micro-scale couplings

The hydro-chemical simulator presented in the previous section can be used to refine the computation of permeability for each timestep and on each sampling point of the mesh at the meso-scale. For each chosen point, this is done in sequential steps illustrated in Fig. 16. The change of porosity $\Delta\phi_{chem}$ stemming from chemical dissolution/precipitation and computed at the meso-scale is transferred to the micro-scale, where it can be used by the erosion/dilation algorithm presented above. The permeability is then upscaled and placed back at the original point of the meso-scale mesh, ready to use for the following timestep.
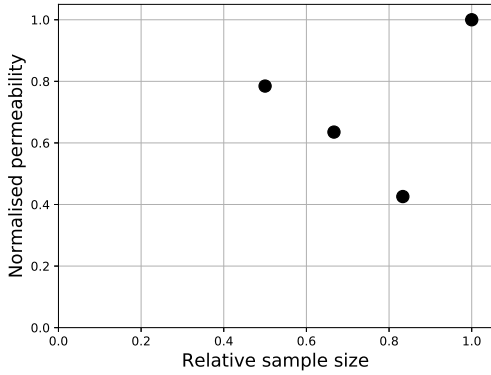
(a) REV non-convergence curve. Both x and y values are normalised with respect to the full-sized sample.
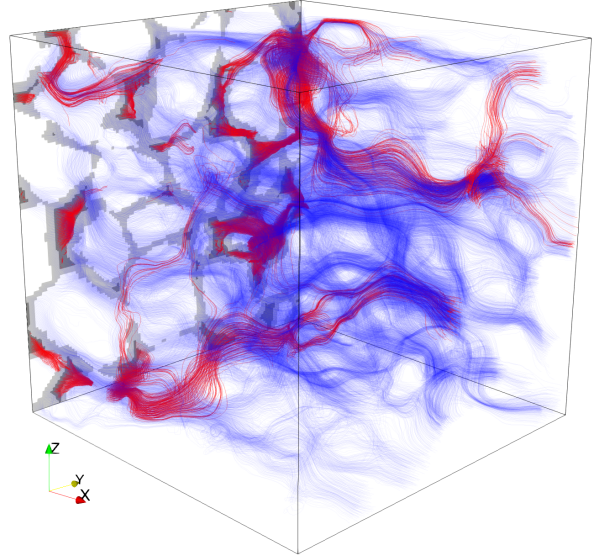
(b) Visualisation of the flow streamlines of both the initial (blue) and the precipitated (red) sample.

Figure 15: Assessment of the REV non-convergence of the LV60A sample of Fig. 14, precipitated to 8% of porosity.

The first section addresses the downscaling of $\Delta\phi_{chem}$ while the second section explains how a smart interpolation is used to upscale the permeability on the whole mesh of the meso-scale with only a few upscaled points of interest.

6.1. Downscaling information from the physical scale

In this framework, the information transferred down from the meso-scale is the evolution of chemical porosity, $\Delta\phi_{chem}$, which is not passed as a boundary conditions but used directly as a target for the erosion/dilation algorithm to get distributed spatially across the mesh of the microstructure. This erosion algorithm is explained in details in Sec. 5.1. Two important aspects, however, are worth mentioning here. Firstly, the erosion algorithm can be qualified of *discrete* in nature. Every element of the mesh is indeed treated in a boolean manner as either grain or pore space, which implies that the distributed porosity cannot be a continuous field. The erosion can then be qualified of discrete in that sense. Secondly, the amount of erosion imposed is applied homogeneously across the whole surface of the pore-grain boundary. Reaching the target $\Delta\phi_{chem}$ is then a matter of eroding or precipitating the appropriate number of layers on that boundary. This discretisation of the erosion affects directly the fitting quality of the porosity evolution in time. Fig. 17 compares the evolution of the (continuous) chemical porosity update requested by the meso-scale with the resulting (discretised) value computed by the erosion algorithm at the micro-scale, highlighting the importance of the mesh resolution for the quality of the fit.

Given the computational time associated with that geometrical erosion algorithm, it is important to note the advantages and drawbacks of the approach. While a coarse discretisation of the porosity can potentially impact negatively the quality of the results, it also presents a considerable performance gain when porosity changes remain limited, which is the case when the fault remains locked (slow creep). Indeed, if the target chemical porosity change is smaller than the corresponding porosity obtained by updating a single layer, then the algorithm leads to no porosity update at all. In order to take advantage of this time-saving feature, we modified the *multiapp* functionality of MOOSE to add this important check at every time step and every downscaling point, before the *multiapp* runs blindly an expensive micro-scale simulation. If the target chemical porosity change is below the minimum threshold, the previous (unchanged) value of permeability gets returned instantaneously. Without a loss of results quality, this smarter multiscaling routine allows to cut down an enormous amount of computational time for two compounded reasons, temporal and spatial.
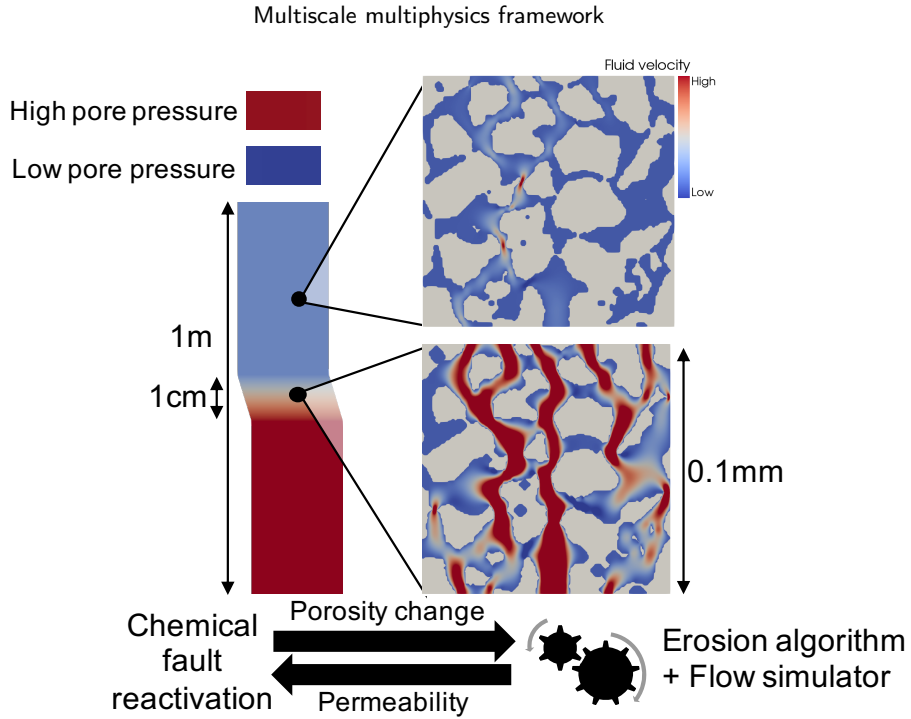
**Figure 16:** Meso/micro-scale model: length scales and couplings.

Firstly, as the fault reactivation is a short event at the production time scale, the fault often remains in its slow creeping (locked) regime. Secondly, the localisation of the deformation within the fault can result in specific zones (and corresponding sampling points) experiencing very little to no chemical alteration, even when the fault reactivates.

6.2. Upscaling properties

As the meso-scale passes a chemical porosity target information to the micro-scale at N sampling points $M_{i\,1 \leq i \leq N}$ where the *mutliapp* is run, the main information transferred back from the micro-scale to the meso-scale is the corresponding value of permeability computed on the eroded or dilated mesh for that timestep. Those updated permeability values at the sampling points M_i then need to be interpolated across the full meso-scale mesh.

A common multiscaling procedure consists in selecting every single Gauss point of the macro-scale mesh as sampling point (Kouznetsova, 2004). The upscaled property is then interpolated naturally on the whole mesh by following the internal finite element interpolation used, linearly for elements of first order or with higher polynomial functions for higher order elements. In comparison, the *multiapp* functionality of MOOSE provides more freedom in the multiscaling procedure as the sampling points can be selected independently from the mesh discretisation. The number and position of the sampling points on the mesh are user-defined and those sampling points do not even need to be located on mesh nodes. Compromise can then be made between computational efficiency and results precision by selecting the location of the sampling points M_i appropriately. For our particular case, given the regular shape of the chemical porosity target across the fault core of the meso-scale observed in Fig. 18, which is essentially one dimensional and symmetrical around the centre of the fault, we can expect a similar permeability profile. This simplifying configuration allows to recreate a permeability profile with an appropriate interpolation scheme and a limited number of sampling points including:

- The middle point of the core zone. This point must be selected as it is experiencing the most drastic change of porosity.

- The far-field boundary condition. The permeability of this reference point only gets computed once at the beginning of every meso-scale simulation since this point sits at the edge of the mesh with a constant temperature boundary condition and does not experience dissolution or precipitation. It is indeed far away from the fault core and all excess heat generated by the localised shear heating gets dissipated by that point.
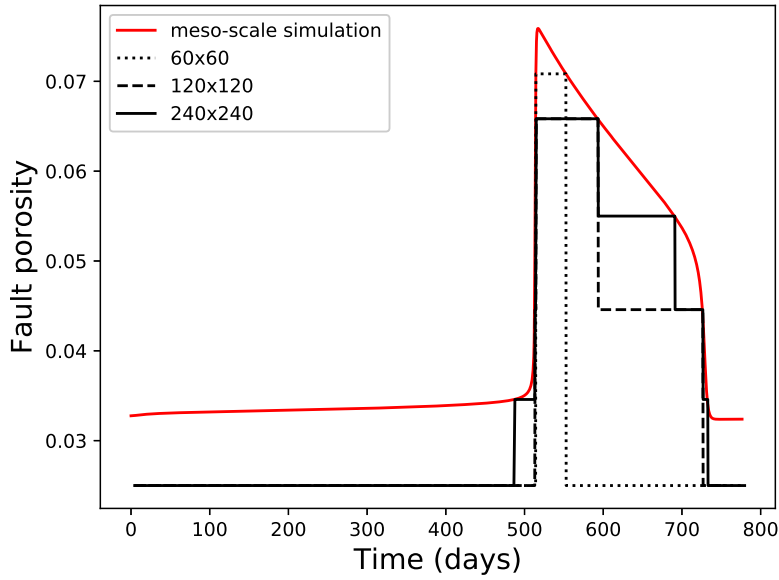
Figure 17: Evolution of the downscaled porosity over time during a fault reactivation for different resolutions $n \times n$ of the micro-scale mesh. The curves are compared to the reference value ϕ computed at the meso-scale.
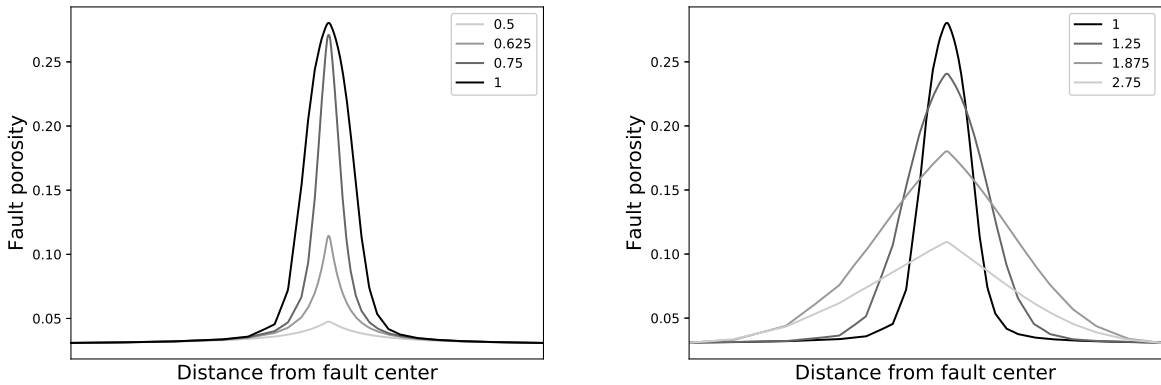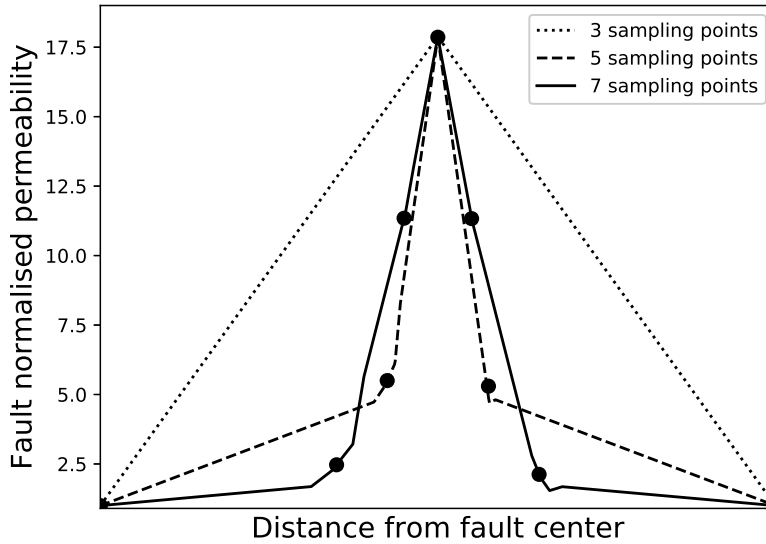

Figure 18: Profiles of porosity across the fault during reactivation (left) and deactivation (right). Times are normalised by the peak reactivation time.

- A few points in between those two. Those points are selected with higher density closer to the middle because of the expected bell curve profile, with the exact number of points depending on the precision required, as shown in Fig. 19.

Note that, despite the symmetrical geometry of the meso-scale mesh, the existence of a pore pressure gradient across the fault breaks the symmetry of the problem, preventing us from using sampling points on a single side of the fault and replicating the symmetrical profile across the centre of the fault. The results show, however, that this pore-pressure contribution remains negligible on the porosity profile, providing a nearly perfectly symmetrical profile nonetheless (see Fig. 18). Therefore, we sample only one half of the fault and we compute the other half by symmetry.

Finally, the interpolation between all sampling points can itself be done in different ways and MOOSE proposes two different options by default: inverse distance weighting and radial basis function interpolation. Those two interpolation

Figure 19: Profiles of permeability across of the fault for increasing sampling. Note that the middle point and the boundary points are sampled in each simulation.

methods are more well suited for 3D cases, so we implemented a simpler linear interpolation to use for the fault transversal profile.

In addition to the macro/meso-scale framework presented before, this section presented the possibility of incorporating yet another scale of importance in the model. Indeed, the information of the rock microstructure is lost at the meso-scale where it is only reduced to the porosity parameter. The only way to retrieve this information is to incorporate the micro-scale in the framework. We focus in this contribution on the effect of chemical alterations on the permeability. This section explained how the multiscaling procedure was done. Because the chemical model is solved at the meso-scale, the downscaled information passed to the micro-scale is directly a chemical porosity change. If this change is small enough, we do not run an expensive upscaling of the permeability since the value would not change much. The permeability is computed on the eroded mesh and transferred back to the sampling points. By adapting the sampling positions to the shape of the expected permeability profile, we can reduce the number of sampling points while keeping a good approximation of the shape of the curve.

7. Application to induced fault reactivation

Previous sections presented three separate scales of importance in the problem of fault reactivation, with the couplings between those scales detailed in Sec 3 and 5. Building on the theoretical presentation of this multiscale multiphysics framework, with all components introduced in the previous chapters, we present now one particular application of this approach for a fluid production-induced chemical fault reactivation. The first sections presents chronologically the different phases of this complex phenomenon (reactivation, propagation, deactivation) which displays a particularly strong interplay between the meso-scale and the macro-scale. The last section demonstrates nonetheless the importance of the micro-scale and how a change in the microstructure can directly affect multiple physical mechanisms at the macro-scale.

7.1. Geological setup

We focus on the problem of a chemically active sealing fault near criticality embedded in a carbonate reservoir under extension as depicted in Figure 6. In accordance with the Andersonian depiction of a typical extensional setting, the fault is dipping at 60° (Anderson, 1905). The reservoir, located at four kilometres depth, measures two hundred

---

Table 1

Parameters for the chemical shear zone model (refer to Sec. 2.1) in the geological environment of Sec. 7.1. We take inspiration from Alevizos et al. (2014); Veveakis et al. (2014) and the references therein as well as L'vov (2007) particularly for the calcite decomposition.

Name	Symbol	Value	Unit
Activation energy of calcite decomposition	E_+	52	$kJ.mol^{-1}$
Activation energy of calcite precipitation	E_-	33	$kJ.mol^{-1}$
Arrhenius number of the mechanics	Ar_m	7	-
Fluid compressibility	β_f	5×10^{-10}	Pa^{-1}
Fluid viscosity	μ_f	0.00023	Pa.s
Molar mass of fluid specy B	M_B	0.018	$kg.mol^{-1}$
Molar mass of solid species A and AB	M_{AB}	0.35	$kg.mol^{-1}$
Pre-exponential factor of forward reaction	A_+	1.4	s^{-1}
Pre-exponential factor of reverse reaction	A_-	0.0014	s^{-1}
Solid density (A and AB)	ρ_s	2700	$kg.m^{-3}$
Taylor-Quinney coefficient	χ	0.6	-
Thermal conductivity of the mixture	α_m	2.7	$kg.m.K^{-1}.s^{-3}$
Thermal diffusivity of the mixture	c_{th}	10^{-6}	$m^2.s^{-1}$

metres in height and stretches horizontally far beyond the fault. We select therefore a zone of 1 km centred on the fault of interest. With the cap rock above and an impermeable layer below, the reservoir is hydraulically sealed at the top and bottom boundaries. In comparison to the 10% porosity and 10 mD permeability of the reservoir, the pre-existing carbonate fault act as a seal with a porosity of 3% (Sulem and Famin, 2009) and a permeability of 0.01 mD. The fault core has a thickness of 1 cm and is modelled at the meso scale (Fig. 2) within 1m of its surroundings. We model the pre-existence of this fault core with a lower strength (16 MPa) than the reservoir (80 MPa). All other properties than the strength and permeability are taken equal within the reservoir and the fault. The reservoir is modelled as an elastic medium with a Young modulus of 20 GPa and a Poisson ratio of 0.2. In order to apply the chemical shear zone model (see Sec. 2.1), we list in addition the specific set of parameters from Table 1.

We impose on the layer the lithostatic overburden stress corresponding to four kilometres depth and we select a vertical to horizontal stress ratio of 2.3 for the reservoir to be in the extensional regime. The pore pressure is initialised with the weight of the hydrostatic column. Given the low background geological strain rate, we assume no lateral displacement of the reservoir during the relatively short time scale of production of a few years. This common hypothesis results in a uniaxial strain loading condition for the reservoir (Jaeger, 2007). Note that the lateral displacements are fixed only after the stress initialisation of the domain in Fig. 20a in order to still capture the extensional nature of the reservoir as can be seen in the setting of Fig. 20b.
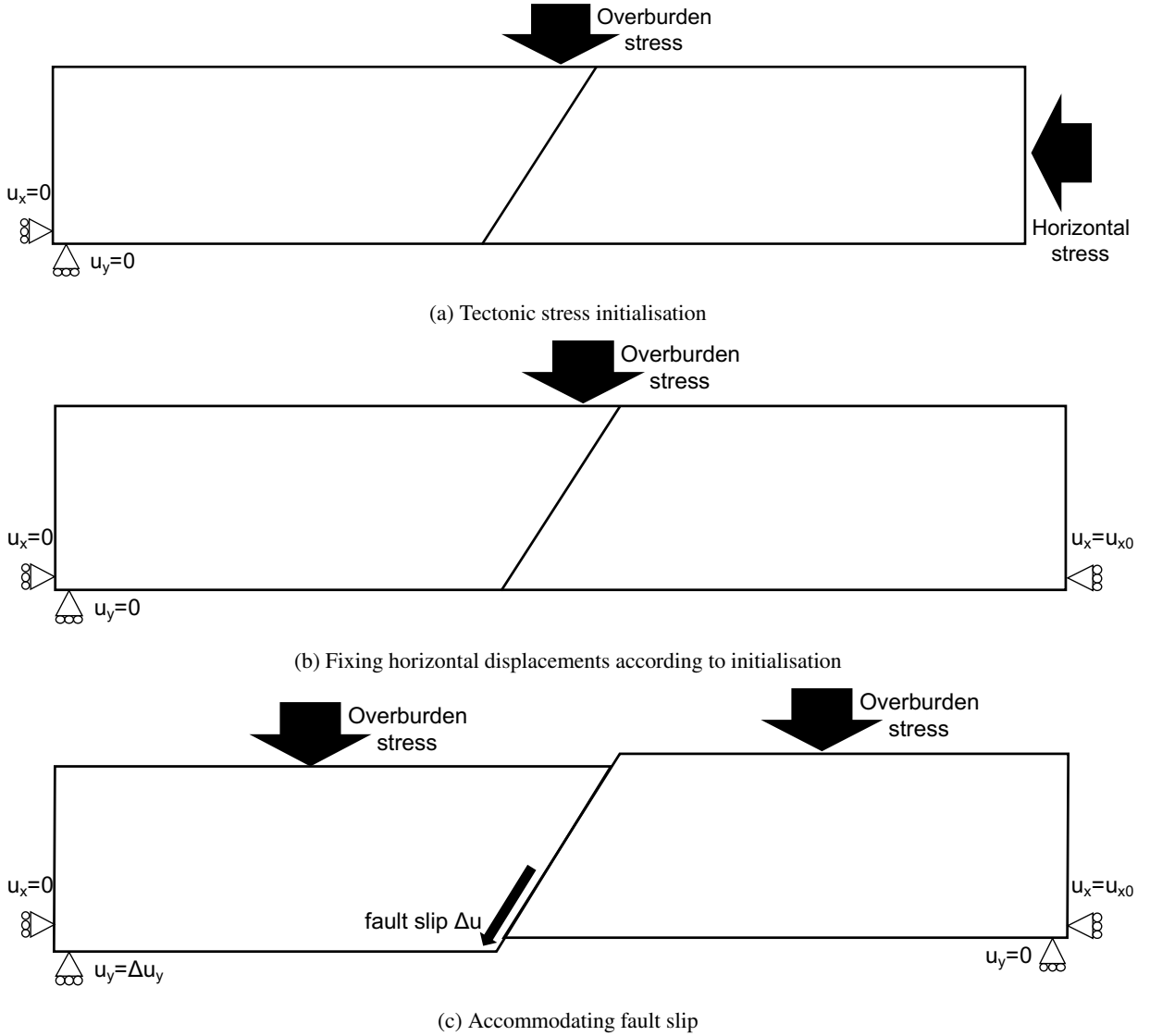
Vertical uplift from a fault slip can propagates far away from the source, sometimes hundreds of kilometres as Scholz (2002, Fig. 5.3) showed for the Nankaido earthquake of 1946. Since this contribution focuses on the local repercussions of the fault reactivation on its environment, we choose to model only a 1 km long section of the reservoir and the vertical slip of the fault is accommodated uniformly across the bottom boundary of the domain on either side of the fault as can be seen in the setting of Fig. 20c. Capturing the effects of the fault slip at the larger scale would require further specific assumptions about the fault surroundings and falls outside the scope of this generic study.

The reservoir is filled with overpressurised oil, of density 0.8, at an initial pore pressure of 40 MPa. Even though the fault permeability is very low, geological times have allowed for the reservoir to equilibrate the pressure on both sides of the fault. From this initial state, we are investigating the fault reactivation scenario in the case of the production from a well drilled through the reservoir located very close to the fault. This section presents the results of the reactivation scenario due to production from a well located next to the sealing fault, as presented in Sec. 7.1. The system displays three important phases: the reactivation of a first fault segment, the propagation of the slip along the fault and finally, the fault deactivation and healing.

7.2. Production-induced fault reactivation

We consider a production well located at 50 m from the fault, as seen on Fig. 6. Initially, the pore pressure is equilibrated on both sides of the fault, despite its low permeability. The simulation starts when oil production begins

(a) Tectonic stress initialisation

(b) Fixing horizontal displacements according to initialisation

(c) Accommodating fault slip

Figure 20: Schematic of boundary conditions. The reservoir, compartmented by a normal fault, is in extension. Note that the stress imposed is total, with the effective stress retrieved with the addition of the pore pressure boundary conditions (imposed hydrostatic gradient on reservoir sides). The pore pressure values are shown indicatively by the colouring of the reservoir in those thee chronological steps, only to help the comprehension of the boundary conditions (see full results in the following sections).

from the well with a prescribed flow rate. Initially, the pressure starts decreasing on the left compartment of the reservoir only, as the fault acts as a seal. Fig. 6 shows the undisturbed pressure distribution across the fault at this early stage of production.

This decrease in pore pressure can potentially lead to fault reactivation, under certain conditions linked to the stress path followed during production and material properties, which can easily be understood with a simple analytical approach. Following the uniaxial strain conditions of the setup considered, known to match field observations of reservoir stress paths (Engelder and Fischer, 1994), the evolution of shear stress $\Delta\tau$ in elasticity can be analytically computed from the variation of pore pressure Δp_f as $\Delta\tau = -\Delta p_f \frac{1-K}{2}$, with $K = \frac{\Delta\sigma_H}{\Delta\sigma_V}$. This ratio K was introduced by Teufel, Rhett and Farrell (1991) to characterise field observations of reservoir stress paths and is expressed as $K = \frac{\nu}{1-\nu}$. For the common model of Coulomb failure criterion used to describe the reactivation of faults, $\tau = c + \mu(\bar{\sigma} - p_f)$.

Therefore, if $\frac{1-K}{2}$ is superior to the friction angle of the fault, then reactivation will ultimately occur (Nacht, De Oliveira, Roehl and Costa, 2010). Our scenario falls under such a case where the shear stress augments with production as pore pressure drops, as seen on Fig. 21d before point A.

This increase of shear stress on the fault links to the generic scenario described in Sec. 2.2 and explains the reactivation of the fault around $t \approx 500$ days, jumping from point A1 to A2 on Fig. 4 which are correspondingly reported on the transient evolution of pore pressure, fault permeability, slip, shear stress and slip velocity plotted in Fig. 21. The jumps in velocity and permeability follow the expected behaviour described in Sec. 2.2. The permeability increase leads to a loss of sealing capability of the fault and lets fluid invade the reservoir. Consequently, the pore pressure on the left-hand side of the fault suddenly jumps (see Fig. 21a), as a result of pressure equilibration to a lower differential across the fault.

7.3. Slip propagation and synchronisation along the fault

The reactivation of the first fault segment occurs at a specific location determined by the heterogeneous stress distribution along the fault, due to the radial diffusion of pressure depletion around the well coupled with gravitational effects. This first slip triggers a cascading chain of events, as the slip of one point of the fault directly impacts the stress state of the neighbouring fault segments. The propagation of slip events is an active field of research (e.g. Lapusta and Rice, 2003; Segall and Pollard, 1983; Reches and Lockner, 1994) and the exhaustive study of all possible scenarios falls outside the scope of this paper. In our particular example, the slip propagates along the whole fault, leading to a complete synchronisation of the fault slippage.

The location of the first slip event corresponds to the zone of highest stress, but, interestingly, it is not directly linked to the pressure depletion profile. Fig. 22 shows this pore pressure profile evolution in time from the start of the simulation as fluid production occurs. It highlights the homothetic transformation of those series of curves and shows that, quickly after the start of production, the minimum of pore pressure shifts from the shallowest point of the fault to the approximate middle of the fault (mid-height of the reservoir), where it remains from that time onwards. Using the stress path explained above, this translates to a maximum shear stress around the middle of the fault, which can be taken as proxy for fault stability, as usually done to assess slip tendency for faults in the plastic regime (Morris, Ferrill and Henderson, 1996). We can then see that the middle of the fault, where the pressure depletion is the highest, has the highest tendency of reactivating. Yet, the multiscale couplings between the fault and the reservoir lead to a more complex problem of interferences between all segments of the fault and we actually observe an initial reactivation of the fault at the top of the model, as can be seen on the timelapse of reactivation in Fig. 23.

Once the first fault segment reactivates, the fault starts slipping, i.e. creeping at a faster rate. The same couplings responsible for the initial reactivation remain at play afterwards and lead to a cascading transfer of forces from that location to the neighbouring fault segments, causing a sequential reactivation of those segments. Slippage is indeed known to propagate much further away than just the surroundings the fault (Scholz, 2002). In order to numerically obtain this phenomenon of propagation, we select some points of interest along the fault where the multiscale couplings stated in Sec. 4 are computed, keeping this number as small as possible for computational purposes, since the full study of the fault slip propagation is out of scope for this contribution. A sensitivity analysis on the number of upscaling points is presented below in Sec. 7.5. In the rest of the section, we still refer to Fig. 21 for clarity, which presents the simulation results with one sampling point taken in the middle of the fault. Following the phase of propagation that ends with the last reactivation event at the bottom of the reservoir, we observe in Fig. 23 a synchronisation of the whole fault.

7.4. Fault deactivation and healing

The slippage of the fault results at the macro-scale in a horizontal elastic relaxation of the reservoir. This stress drop tends to bring back the fault towards a deactivated state, competing with the pressure depletion which keeps it activated. Given the difference of rates of those two processes, with pressure diffusing much slower than the fault slips, the stress decreases faster than the strain rate increases. This relaxation decreases the shearing stress at the fault, which corresponds to tracing downwards the highest branch of Fig. 21d from the reactivated state (point A2). After a sufficient decrease, the stress reaches a low enough value (point B1) where the fault cannot remain in its activated state and returns to the lower branch of the S-curve (drop from point B1 to B2). The temperature and slip velocity return to their initial value (see Fig. 21e) and the fault goes back to its initial slow creep regime. Correspondingly, the permeability goes back to its initial low value (see Fig. 21b) as the reversible temperature-activated calcite decomposition reaction switches from forward to reverse direction. The chemical dissolution responsible for the large increase of permeability

gives way to its opposite reaction, which heals the fault by precipitating calcite at its core.

For the generic scenario selected, the whole reactivation event lasts for 250 days. Note the small thickness of reservoir leads the slip to propagate to the limits of the domain and the whole reservoir therefore accommodates the same vertical displacement jump as the fault. The fact that the reactivated fault splits the whole reservoir leads to an artificially increased period of slip. Considering a much deeper section of the reservoir, as well as its 3D nature, would be required to model appropriately a more precise duration of the whole slip event. This example illustrates nonetheless the ability of the approach to capture the physical couplings responsible for the activation, permeability increase and deactivation. Nonetheless, we expect a longer opening compared to a brittle fault slip, characteristic of ductile faults, along with an aseismic slip (velocity of 10^{-11}m.s^{-1} in Fig. 21e).

7.5. Sensitivity analysis on upscaling points sampling

We investigate the sparsest sampling of upscaling points required to approach the full solution where all mesh points of the faults would be used to compute the macro/meso-scale coupling. Fig. 24 shows the results of different configurations used to run the same simulation with 1, 2, 3 and 5 upscaling points at different positions along the fault. The property used to visualise the convergence of the solution with the number of upscaling points is both the reactivation onset and the opening time of the fault. Note that all configurations led to the same qualitative result, with the top segment of the fault reactivating first and a synchronisation of slippage for the whole fault across the full thickness of the reservoir.

We can see that our reduced system respects the full system behaviour as long as the top and middle segments are included in the upscaling, for which the reactivation onset happens at ≈150 days and the fault stays open for ≈300 days. Increasing furthermore the number of points shows that it increases slightly the precision of the solution but the relative error on the solution has already qualitatively converged for 3 points of upscaling.

Results of the simulation using a representative number of sampling points (five) are visualised in Fig. 26, displaying all phases of the reactivation event as a visual summary of this section. Fig. 26a displays the sealing characteristic of the fault through the pressure discontinuity at the interface and the small arrows of fluid velocity in the right-hand side compartment of the reservoir. After a first reactivation event, at the top of the fault, the reactivation propagates downwards. Particularly, we visualise in Fig. 26b the moment when the propagation reaches the middle of the fault. The large arrows of fluid velocity indicate that the top segment has already reactivated, whereas the bottom segment remains sealed. The peak of fluid velocity located at the middle of the fault corresponds to the peak observed during propagation in Fig. 23. Following the phase of propagation, the synchronisation of the whole fault is observed in Fig. 26c, characterised by visible fault slippage and large arrows of fluid velocity along the whole fault. Healing occurs as the last phase and Fig. 26d displays a similar state as Fig. 26a with, however, an advanced stage of pressure depletion and the fault slippage accumulated during the reactivation event.

Interestingly, when considering multiple points of upscaling and obtaining this event of propagation, the whole behaviour of the fault is different from the one obtained with a single point, as the phenomenon becomes one dimensional in space along the fault. If we do monitor the point in the middle of the fault, see Fig. 25, we can observe the interferences from other fault segments during the propagation event. They are visible on the plots of Fig. 25 as a perturbation of the curves of Fig. 21 around point A. This noise lasts for ≈15% of the full event and after synchronisation, the behaviour becomes similar to the solution with one sampling point. Therefore, in order to keep a clear visualisation of the phenomena for the purpose of theoretical understanding, we display later in the contribution cases computed with only one sampling point in the middle of the fault.

7.6. Influence of the microstructure on the system

The coupled macro/meso-scale framework of Sec. 4 was used in the previous section to simulate an induced chemical fault reactivation event. Having understood the complex interplay between the macro- and meso-scales, we add to the framework the micro-scale couplings described in Sec. 6 and summarised by Fig. 16, in order to refine the evolution of the permeability of the fault. The consideration of the micro-scale allows us to study the influence of the microstructure on the whole multiscale phenomenon, which is done in this section by comparing the effect of two different microstructures.

We consider two different synthetic microstructures, α and β, represented directly by their flow path, shown respectively in Fig. 27a and Fig. 27d. Both microstructures have the same porosity and tortuosity (the flow path has the same length), therefore the same permeability. As such, these two configurations would be strictly identical at the meso-scale if the porosity and permeability were the only properties considered in the upscaling process. Yet, we

can show a major difference of behaviour between those two microstructures when subjected to the same arbitrary cycle of dissolution and re-precipitation, as induced by fault reactivation and deactivation events. Fig. 27b (resp. 27e) shows the eroded microstructure α (resp. β) after dissolution and Fig. 27c (resp. 27f) the final dilated configuration after the re-precipitation step. We observe that the narrow gap between the vertical channels of microstructure β gets completely eroded during the dissolution process when the porosity reaches a value of $\approx 18\%$, connecting the two horizontal channels and leading to a shorter flow path.

The two microstructures α and β are now linked to the meso- and macro-scales simulations of the case study of Sec. 7.1 and the outputs are plotted on Fig. 28 for the pore pressure, permeability, slip, shear stress and slip velocity, in blue (resp. red) for microstructure α (resp. β). Until the reactivation, both sets of curves superpose perfectly since the initial permeabilities of the two microstructures are equal.

At the peak of reactivation, however, microstructure β has reached a higher permeability from the new channel opening (see Fig. 27e). This higher permeability results in a more pronounced pressure equilibration, as seen in Fig. 28a for microstructure β ($t\approx 300$ days). Following the stress path described in Sec. 7.4, a higher pore pressure translates to an increase in Von Mises stress, which keeps the fault activated for a longer period as observed in Fig. 28e-28c.

This comparative study shows clearly that a change of geometry at the micro-scale, unnoticeable with the restrictive characterisation of microstructure through the notions of porosity and permeability only, affects different physical aspects of the behaviour at the macro-scale. The dependency on the microstructure is achieved with our framework through a complex coupling effect of scales and physical mechanisms, as visualised in the simplified diagram of Fig. 1b. Pressure depletion due to production increases the shear stress at the fault due to the stress path. Past a stress threshold, the fault reactivates and slips. Simultaneously, chemical dissolution is triggered and the two microstructures reach a different permeability. This permeability feeds back into Darcy's law at the macro-scale and leads to a different pressure equilibration, which in turns changes the fault deactivation time due to the stress path.

8. Summary and conclusions

This contribution presented a three-scale multiphysics approach that successfully simulates a chemical fault reactivation and showed the importance of dynamically-upscaled laws, when the use of empirical laws can be too specific to a particular configuration and lack information from the lower scales. The phenomenon of permeability increase during such a fault reactivation was shown to be complex, because of the strong couplings between all physical mechanisms at play, such as chemical dissolution, shear heating, mechanical deformation and pressure diffusion occurring across the various scales of the system. We introduced the components and framework required to couple all physical processes at their appropriate scales of interest. All elements were then used together in Sec 7 to model a generic geological scenario, reproducing in a single simulation all characteristic aspects expected for such a phenomenon: material instability, aseismic slip, permeability increase, elastic stress relaxation, deactivation, healing

An important particularity of this multiscale framework is the master role of the meso (m) scale, which corresponds to the physical length scale of the chemical fault reactivation phenomenon. This approach contrasts from the common fault reactivation modelling done at the reservoir scale (e.g. Cappa and Rutqvist, 2011) and the mechanical studies on localisation purely upscaled from the micro-scale (e.g. Nitka et al., 2011). The meso-scale was shown to capture adequately the chemical shear zone behaviour, which is applicable to high P,T environments, where chemistry becomes more active. While fault reactivation in such deep environments might suffer from a lack of data compared to brittle faults found at shallower depths, their study is actually more tractable because of the driving influence of the physics governing the system, compared to shallower systems which are more strongly influenced by geometrical and material heterogeneities. For a given setup, the stability of a ductile system depends solely on its material properties and can be derived using an arc length continuation method (Sec. 2.2), which provides a full description of the possible states of the fault. For instance, this analysis had previously helped validate the chemical shear zone (CSZ) model against real data in drastic environments like subduction zones (Alevizos et al., 2014; Veveakis et al., 2014; Poulet et al., 2014a) or megathrusts (Poulet et al., 2014b), identifying an episodic oscillatory behaviour of such stick-slip faults.

This framework extends the CSZ model's range of applications to more complex behaviours at the macro-scale where the boundary conditions at the fault evolve with time. Previous applications of that model had indeed been limited to static boundary conditions corresponding to tectonic forces (e.g. Alevizos et al., 2014; Veveakis et al., 2014; Poulet et al., 2014a,b; Poulet and Veveakis, 2016). However, in the case of fluid production in the reservoir, the stress state of the fault depends strongly on the level of depletion of the reservoir. To take this into account, we introduced the reservoir scale (macro, Sec. 3) to simulate through poromechanics the stress changes along the fault stemming from

fluid production. The macro-scale is used to provide the boundary conditions of stress and pressure to the meso-scale at every time step. Due to the clear scale separation, the fault can be treated as an interface at the macro-scale. Compared to common cases where the fault is either treated as a channel or a seal, we need to be able to treat both states and the continuous transitions in-between. Our interface law presented in Sec. 3.2 handles all configurations by directly resolving the flow through the fault. After the meso-scale resolution, changes of permeability and increase of slippage are fed back to the interface law of the meso-scale. By doing so, the consequences of fault reactivation such as fluid invasion can be studied at the macro-scale. Particularly, we showed in Sec. 7.4 that the increasing slippage results in an elastic stress relaxation of the reservoir and leads to the fault deactivation which was previously only artificially taken into account for empirical laws (e.g. Cueto-Felgueroso, Vila, Santillán and Mosquera, 2018).

Sec 7's case study displayed the model's ability to predict the occurrence of the reactivation, which is the critical parameter needed for safe subsurface operations. By coupling strongly all the physical mechanisms at play, our model is able to resolve continuously the instability of temperature that controls the phenomenon. The transition between locked and active regimes of the fault happens therefore smoothly, yet in a very short amount of time, matching nicely an artificial switch between regimes used more commonly in fault reactivation models. This same smooth but sharp transition occurs in the deactivation stage.

We suggest that the extraordinarily high permeability increase observed during some fault reactivation can be physically modelled with the consideration of chemical dissolution, which is active for deep carbonate rocks. Instead of a difficult calibration of an empirical law, with the aperture of the fractures vs the shear strain for example, the permeability increase can be quantified in our model using the chemical properties of the fault gouge which could be measured from cores. Coupled with the finite duration of the reactivation event, the change of permeability results in a temporary loss of the fault seal. Consequently, the model can compute the amount of fluid that leaked through the fault which provides a good assessment of the consequences of the reactivation event.

The consideration of the micro-scale in the multiscale framework (Sec 6) comes as an effort to link the field of data-driven science to physics-based modelling in the sense that the microstructural data, collected to characterise rock properties, is used quantitatively for physical modelling in this contribution, in a dynamical hydro-chemical simulation to simulate the transient evolution of permeability with deformation. Sec. 7.6's study showcased strongly the influence of multiphysics couplings across scales and highlighted how to account for simple changes in the microstructure from μCT-scans and quantitatively assess the resulting impact on the duration of the reactivation event at the macro-scale.

The framework introduced in this thesis is particularly rich in applications and opened the door to further exciting studies. For instance, while the study of Sec. 7 focused mainly on chemical alterations as the preponderant deformation mechanism of the microstructure, mechanical deformations remain non-negligible during fault reactivation, especially for the shear component, and affect as well the geometry of the microstructure. The permeability upscaling of Sec. 7 could therefore be further refined when linked with the hydro-mechanical simulator developed by Lesueur et al. (2017) to capture other effects and link microstructural geological observations to the overall fault reactivation process.

The overall modelling framework was illustrated on a specific application to production-induced fault reactivation, yet it remains much more generic and flexible to capture numerous other scenarios linked to fault reactivation. Within the context of petroleum engineering, fluid injection is actually the most common cause for fault reactivation and could just as well be modelled with this approach. Implementing more physics at the macro-scale could also easily diversify the range of applications, including geothermal exploration, enhanced oil recovery or CO_2 storage. At even larger length scales and geological timescales, this framework is also applicable to plate tectonics theory looking at purely tectonic perturbations of faults. In this context, the framework can also be applied to mineral exploration, extending preliminary results from Poulet, Lesueur, Hue, Veveakis and Regenauer-Lieb (2018a); Poulet, Lesueur, Veveakis and Regenauer-Lieb (2018b) where fault openings are inferred to cause the episodic propagation of mineralising fluids, responsible for giant ore deposits when they reach lower P,T environments. This modelling framework captures the evolution of multi-physical processes across scales in a way that was unforeseeable previously and opens to door to truly exciting studies in a wide range of fields.

Computer code availability

All results presented in this study were obtained with the open-source REDBACK simulator (Poulet et al., 2017) (`http://github.com/pou036/redback`), a MOOSE module (Gaston, Newman, Hansen and Lebrun-Grandié, 2009).

Table 2
Table of symbols

Symbol	Name	Unit of measure
Ar	Arrhenius number	-
K	Kozeny constant	-
Re	Reynolds number	-
α	Thermal conductivity	$kg.m.K^{-1}.s^{-3}$
β	Compressibility	Pa^{-1}
χ	Taylor-Quinney coefficient	-
ε	Solid strain	-
κ	Permeability	m^2
λ	Thermal expansion coefficient	K^{-1}
ω	Molar reaction rates	$mol.m^{-3}.s^{-1}$
μ	Friction	-
μ_f	Fluid viscosity	$Pa.s$
ν	Poisson Ratio	-
ϕ	Porosity	-
ψ	Test function	-
Φ	Trial function	-
ρ	Density	$kg.m^{-3}$
σ	Solid stress tensor	Pa
τ	Shear stress	Pa
ϑ	Relaxation factor	-
A	Pre-exponential factor	s^{-1}
C_p	Specific heat capacity	$m^2.K^{-1}.s^{-2}$
c	Cohesion	Pa
d_s	Grain/sphere diameter	m
D	Thickness	m
E	Young's modulus	Pa
$E_{+,-}$	Activation energy of forward or reverse reaction	$J.mol^{-1}$
g	Standard gravity	$m.s^{-2}$
H_F	Fault thickness	m
h	Height	m
k	Permeability	D
L	Length	m
M	Molar mass	$kg.mol^{-1}$
n	Normal unit vector	-
p_f	Fluid pressure	Pa
p	Mean stress	Pa
q	Von Mises stress	Pa
R	Gas constant	$J.K^{-1}.mol^{-1}$
S	Specific surface area	m^{-1}
s	Solid ratio	-
T	Temperature	$°C$
t	Traction	Pa
u	Displacement	m
V	Volume	m^3
v	Velocity	$m.s^{-1}$
w	Tangent unit vector	-
$\cdot^*$	Normalised variables	-
$\cdot^{ref}$	Reference values	-
X_m	Mixture average	$(1 - \phi)X_s + \phi X_f$

References

Alevizos, S., Poulet, T., Veveakis, E., 2014. Thermo-poro-mechanics of chemically active creeping faults. 1: Theory and steady state considerations. Journal of Geophysical Research: Solid Earth 119, 4558–4582. doi:10.1002/2013JB010070.

Anderson, E.M., 1905. The dynamics of faulting. Transactions of the Edinburgh Geological Society 8, 387–402. doi:10.1144/transed.8.3.387.

Andrä, H., Combaret, N., Dvorkin, J., Glatt, E., Han, J., Kabel, M., Keehm, Y., Krzikalla, F., Lee, M., Madonna, C., Marsh, M., Mukerji, T., Saenger, E.H., Sain, R., Saxena, N., Ricker, S., Wiegmann, A., Zhan, X., 2013. Digital rock physics benchmarks—part II: Computing effective properties. Computers & Geosciences 50, 33–43. doi:10.1016/j.cageo.2012.09.008.

Andrews, D.J., 1976. Rupture velocity of plane strain shear cracks. J. Geophys. Res. 81, 5679–5687. doi:10.1029/jb081i032p05679.

Arns, C., 2009. Structure-property Relationships from Digital Images. VDM Verlag. URL: https://www.ebook.de/de/product/8210630/christoph_arns_structure_property_relationships_from_digital_images.html.

Bandis, S., Lumsden, A., Barton, N., 1983. Fundamentals of rock joint deformation. International Journal of Rock Mechanics and Mining Sciences & Geomechanics Abstracts 20, 249–268. doi:10.1016/0148-9062(83)90595-8.

Bear, J., 1972. Dynamics of fluids in porous media (Environmental science series). American Elsevier Publishing.

Blunt, M.J., Bijeljic, B., Dong, H., Gharbi, O., Iglauer, S., Mostaghimi, P., Paluszny, A., Pentland, C., 2013. Pore-scale imaging and modelling. Adv. Water Resour. 51, 197–216. doi:10.1016/j.advwatres.2012.03.003.

Bratu, G., 1914. Sur les équations intégrales non linéaires. Bulletin de la Société Mathématique de France 42, 113–142. URL: http://www.numdam.org/item/BSMF_1914__42__113_0, doi:10.24033/bsmf.943.

Brinkman, H.C., 1949. A calculation of the viscous force exerted by a flowing fluid on a dense swarm of particles. Flow, Turbulence and Combustion 1, 27. doi:10.1007/bf02120313.

Burchette, T.P., 2012. Carbonate rocks and petroleum reservoirs: a geological perspective from the industry. Geological Society, London, Special Publications 370, 17–37. doi:10.1144/sp370.14.

Cappa, F., Rutqvist, J., 2011. Modeling of coupled deformation and permeability evolution during fault reactivation induced by deep underground injection of CO2. Int. J. Greenhouse Gas Control 5, 336–346. doi:10.1016/j.ijggc.2010.08.005.

Chapuis, R.P., Aubertin, M., 2003. On the use of the kozeny–carman equation to predict the hydraulic conductivity of soils. Canadian Geotechnical Journal 40, 616–628. doi:10.1139/t03-013.

Cleary, P.W., Pereira, G.G., Lemiale, V., Delle Piane, C., Clennell, M.B., 2015. Multiscale model for predicting shear zone structure and permeability in deforming rock. Computational Particle Mechanics 3, 179–199. doi:10.1007/s40571-015-0073-4.

Correa, A.C.F., Newman, R.B., Naveira, V.P., Serra de Souza, A.L., Araujo, T., da Silva, A.A.C., Soares, A.C., Herwanger, J.V., Meurer, G.B., 2013. Integrated modeling for 3d geomechanics and coupled simulation of fractured carbonate reservoir, in: OTC Brasil, Offshore Technology Conference. doi:10.4043/24409-ms.

Cueto-Felgueroso, L., Vila, C., Santillán, D., Mosquera, J.C., 2018. Numerical modeling of injection-induced earthquakes using laboratory-derived friction laws. Water Resour. Res. 54, 9833–9859. doi:10.1029/2017wr022363.

Desrues, J., Argilaga, A., Pont, S.D., Combe, G., Caillerie, D., kein Nguyen, T., 2017. Restoring mesh independency in FEM-DEM multi-scale modelling of strain localization using second gradient regularization, in: Springer Series in Geomechanics and Geoengineering. Springer International Publishing, pp. 453–457. doi:10.1007/978-3-319-56397-8_57.

Dieterich, J.H., 1979. Modeling of rock friction: 1. experimental results and constitutive equations. J. Geophys. Res. 84, 2161–2168. doi:10.1029/jb084ib05p02161.

Dos Santos, M.D.L., Oliveira, F.R., 2014. Fault reactivation as mechanism of early water production in unconsolidated sandstones reservoirs, in: SPE Annual Technical Conference and Exhibition, Society of Petroleum Engineers. doi:10.2118/170850-ms.

Doyen, P.M., 1988. Permeability, conductivity, and pore geometry of sandstone. J. Geophys. Res. 93, 7729. doi:10.1029/jb093ib07p07729.

Engelder, T., Fischer, M.P., 1994. Influence of poroelastic behavior on the magnitude of minimum horizontal stress, sh in overpressured parts of sedimentary basins. Geology 22, 949–952. doi:10.1130/0091-7613(1994)022<0949:iopbot>2.3.co;2.

Ergun, S., Orning, A.A., 1949. Fluid flow through randomly packed columns and fluidized beds. Industrial & Engineering Chemistry 41, 1179–1184. doi:10.1021/ie50474a011.

Faulkner, D., Jackson, C., Lunn, R., Schlische, R., Shipton, Z., Wibberley, C., Withjack, M., 2010. A review of recent developments concerning the structure, mechanics and fluid flow properties of fault zones. J. Struct. Geol. 32, 1557–1575. doi:10.1016/j.jsg.2010.06.009.

Gaston, D., Newman, C., Hansen, G., Lebrun-Grandié, D., 2009. MOOSE: A parallel computational framework for coupled systems of nonlinear equations. Nucl. Eng. Des. 239, 1768–1778. doi:10.1016/j.nucengdes.2009.05.021.

Heijs, A.W.J., Lowe, C.P., 1995. Numerical evaluation of the permeability and the kozeny constant for two types of porous media. Physical Review E 51, 4346–4352. doi:10.1103/physreve.51.4346.

Hill, R., 1963. Elastic properties of reinforced solids: Some theoretical principles. J. Mech. Phys. Solids 11, 357–372. doi:10.1016/0022-5096(63)90036-x.

Holland, A.A., 2013. Earthquakes triggered by hydraulic fracturing in south-central oklahoma. Bull. Seismol. Soc. Am. 103, 1784–1792. doi:10.1785/0120120109.

Imperial College Consortium On Pore-Scale Modelling, 2014a. C1 carbonate. doi:10.6084/m9.figshare.1189257.

Imperial College Consortium On Pore-Scale Modelling, 2014b. Lv60a sandpack. doi:10.6084/m9.figshare.1153795.

Jaeger, J.C., 2007. Fundamentals of Rock Mechanics. Wiley-Blackwell.

Jolley, S.J., Fisher, Q.J., Ainsworth, R.B., 2010. Reservoir compartmentalization: an introduction. Geological Society, London, Special Publications 347, 1–8. doi:10.1144/sp347.1.

Keller, H.B., 1977. Numerical solution of bifurcation and nonlinear eigenvalue problems, applications of bifurcation theory. Numerical Solution of Bifurcation and Nonlinear Eigenvalue Problems , 359–384.

Keranen, K.M., Weingarten, M., Abers, G.A., Bekins, B.A., Ge, S., 2014. Sharp increase in central oklahoma seismicity since 2008 induced by massive wastewater injection. Science 345, 448–451. doi:10.1126/science.1255802.

Kouznetsova, V.G., 2004. Computational homogenization for the multi-scale analysis of multi-phase materials. phdthesis. Technische Universiteit Eindhoven. doi:10.6100/IR560009.

Lapusta, N., Rice, J.R., 2003. Nucleation and early seismic propagation of small and large events in a crustal earthquake model. Journal of Geophysical Research: Solid Earth 108. doi:10.1029/2001jb000793.

Lesueur, M., Casadiego, M.C., Veveakis, M., Poulet, T., 2017. Modelling fluid-microstructure interaction on elasto-visco-plastic digital rocks. Geomechanics for Energy and the Environment 12, 1–13. doi:10.1016/j.gete.2017.08.001.

L'vov, B., 2007. Thermal Decomposition of Solids and Melts. volume 7 of *Hot Topics in Thermal Analysis and Calorimetry*. Springer-Verlag GmbH. URL: https://www.ebook.de/de/product/11432799/boris_v_l_vov_thermal_decomposition_of_solids_and_melts.

html, doi:10.1007/978-1-4020-5672-7.

Morin, R.H., 2006. Negative correlation between porosity and hydraulic conductivity in sand-and-gravel aquifers at cape cod, massachusetts, USA. J. Hydrol. 316, 43–52. doi:10.1016/j.jhydrol.2005.04.013.

Morris, A., Ferrill, D.A., Henderson, D.B., 1996. Slip-tendency analysis and fault reactivation. Geology 24, 275. doi:10.1130/0091-7613(1996) 024<0275:staafr>2.3.co;2.

Mostaghimi, P., Blunt, M.J., Bijeljic, B., 2012. Computations of absolute permeability on micro-CT images. Math. Geosci. 45, 103–125. doi:10.1007/s11004-012-9431-4.

Nacht, P.K., De Oliveira, M., Roehl, D.M., Costa, A.M., 2010. Investigation of geological fault reactivation and opening. Mecánica Computacional XXIX, 8687–8697.

Nitka, M., Combe, G., Dascalu, C., Desrues, J., 2011. Two-scale modeling of granular materials: a DEM-FEM approach. Granular Matter 13, 277–281. doi:10.1007/s10035-011-0255-6.

Olsson, R., Barton, N., 2001. An improved model for hydromechanical coupling during shearing of rock joints. Int. J. Rock Mech. Min. Sci. 38, 317–329. doi:10.1016/s1365-1609(00)00079-4.

Peterie, S.L., Miller, R.D., Intfen, J.W., Gonzales, J.B., 2018. Earthquakes in kansas induced by extremely far-field pressure diffusion. Geophys. Res. Lett. 45, 1395–1401. doi:10.1002/2017gl076334.

Poulet, T., Lesueur, M., Hue, L., Veveakis, M., Regenauer-Lieb, K., 2018a. Modelling the formation of bonanza-grade ore deposits, in: TIGeR Conference.

Poulet, T., Lesueur, M., Veveakis, M., Regenauer-Lieb, K., 2018b. Propagating mineralising fluids through chemical shear zones, in: AGU Fall Meeting.

Poulet, T., Paesold, M., Veveakis, M., 2017. Multi-physics modelling of fault mechanics using redback: A parallel open-source simulator for tightly coupled problems. Rock Mech. Rock Eng. 50, 733–749. URL: https://doi.org/10.1007/s00603-016-0927-y, doi:10.1007/s00603-016-0927-y.

Poulet, T., Veveakis, E., Regenauer-Lieb, K., Yuen, D.A., 2014a. Thermo-poro-mechanics of chemically active creeping faults: 3. the role of serpentinite in episodic tremor and slip sequences, and transition to chaos. Journal of Geophysical Research: Solid Earth 119, 4606–4625. doi:10.1002/2014JB011004.

Poulet, T., Veveakis, M., 2016. A viscoplastic approach for pore collapse in saturated soft rocks using REDBACK: An open-source parallel simulator for rock mEchanics with dissipative feedBACKs. Comput. Geotech. 74, 211–221. doi:10.1016/j.compgeo.2015.12.015.

Poulet, T., Veveakis, M., Herwegh, M., Buckingham, T., Regenauer-Lieb, K., 2014b. Modeling episodic fluid-release events in the ductile carbonates of the glarus thrust. Geophys. Res. Lett. 41, 7121–7128. doi:10.1002/2014gl061715.

Reches, Z., Lockner, D.A., 1994. Nucleation and growth of faults in brittle rocks. Journal of Geophysical Research: Solid Earth 99, 18159–18173. doi:10.1029/94jb00115.

Regenauer-Lieb, K., Yuen, D.A., 1998. Rapid conversion of elastic energy into plastic shear heating during incipient necking of the lithosphere. Geophys. Res. Lett. 25, 2737–2740. doi:10.1029/98GL02056.

Rice, J.R., 2006. Heating and weakening of faults during earthquake slip. Journal of Geophysical Research: Solid Earth 111. doi:10.1029/2005jb004006.

Scheidegger, A.E., 1974. The physics of flow through porous media. University of Toronto Press. URL: https://www.amazon.com/physics-flow-through-porous-media/dp/0802018491?SubscriptionId=AKIAIOBINVZYXZQZ2U3A&tag=chimbori05-20&linkCode=xm2&camp=2025&creative=165953&creativeASIN=0802018491.

Scholz, C.H., 2002. The Mechanics of Earthquakes and Faulting. Cambridge University Press. doi:10.1017/cbo9780511818516.

Segall, P., 1989. Earthquakes triggered by fluid extraction. Geology 17, 942–946. doi:10.1130/0091-7613(1989)017<0942:etbfe>2.3.co;2.

Segall, P., Grasso, J.R., Mossop, A., 1994. Poroelastic stressing and induced seismicity near the lacq gas field, southwestern france. J. Geophys. Res. 99, 15423–15438. doi:10.1029/94jb00989.

Segall, P., Pollard, D.D., 1983. Nucleation and growth of strike slip faults in granite. J. Geophys. Res. 88, 555. doi:10.1029/jb088ib01p00555.

Sibson, R.H., Robert, F., Poulsen, K.H., 1988. High-angle reverse faults, fluid-pressure cycling, and mesothermal gold-quartz deposits. Geology 16, 551–555. doi:10.1130/0091-7613(1988)016<0551:harffp>2.3.co;2.

Serra de Souza, A.L., Lima Falcão, F.O., 2015. R&d in reservoir geomechanics in brazil: Perspectives and challenges, in: OTC Brasil, Offshore Technology Conference. doi:10.4043/26205-ms.

Sulem, J., Famin, V., 2009. Thermal decomposition of carbonates in fault zones: Slip-weakening and temperature-limiting effects. J. Geophys. Res. 114. doi:10.1029/2008jb006004.

Terzaghi, K.v., 1923. Die berechnung der durchlassigkeitsziffer des tones aus dem verlauf der hydrodynamischen spannungserscheinungen 132, 125–138.

Teufel, L.W., Rhett, D.W., Farrell, H.E., 1991. Effect of reservoir depletion and pore pressure drawdown on in situ stress and deformation in the ekofisk field, north sea, in: The 32nd U.S. Symposium on Rock Mechanics (USRMS), American Rock Mechanics Association.

Tung, R., Poulet, T., Alevizos, S., Veveakis, E., Regenauer-Lieb, K., 2017. Shear heating in creeping faults changes the onset of convection. Geophys. J. Int. 211, 270–283. doi:10.1093/gji/ggx295.

Veveakis, E., Alevizos, S., Poulet, T., 2017. Episodic tremor and slip (ETS) as a chaotic multiphysics spring. Phys. Earth Planet. Inter. 264, 20–34. doi:10.1016/j.pepi.2016.10.002.

Veveakis, E., Alevizos, S., Vardoulakis, I., 2010. Chemical reaction capping of thermal instabilities during shear of frictional faults. J. Mech. Phys. Solids 58, 1175–1194. doi:10.1016/j.jmps.2010.06.010.

Veveakis, E., Poulet, T., Alevizos, S., 2014. Thermo-poro-mechanics of chemically active creeping faults: 2. transient considerations. Journal of Geophysical Research: Solid Earth 119, 4583–4605. doi:10.1002/2013jb010071.

Wang, K., Sun, W., 2018. A multiscale multi-permeability poroplasticity model linked by recursive homogenizations and deep learning. Comput. Methods Appl. Mech. Eng. 334, 337–380. doi:10.1016/j.cma.2018.01.036.

Wibberley, C.A.J., Yielding, G., Di Toro, G., 2008. Recent advances in the understanding of fault zone internal structure: a review. Geological Society, London, Special Publications 299, 5–33. doi:10.1144/sp299.2, arXiv:https://sp.lyellcollection.org/content/299/1/5.full.pdf.

Wilson, M.P., Foulger, G.R., Gluyas, J.G., Davies, R.J., Julian, B.R., 2017. HiQuake: The human-induced earthquake database. Seismol. Res. Lett. 88, 1560–1565. doi:10.1785/0220170112.

Wiprut, D., Zoback, M.D., 2000. Fault reactivation and fluid flow along a previously dormant normal fault in the northern north sea. Geology 28, 595–598. doi:10.1130/0091-7613(2000)28<595:fraffa>2.0.co;2.

Wong, R., Li, Y., 2001. A deformation-dependent model for permeability changes in oil sand due to shear dilation. J. Can. Pet. Technol. 40. doi:10.2118/01-08-03.

Yoon, H., Kang, Q., Valocchi, A.J., 2015. Lattice boltzmann-based approaches for pore-scale reactive transport. Rev. Mineral. Geochem. 80, 393–431. doi:10.2138/rmg.2015.80.12.

Zhang, Y., Clennell, M.B., Delle Piane, C., Ahmed, S., Sarout, J., 2016. Numerical modelling of fault reactivation in carbonate rocks under fluid depletion conditions – 2d generic models with a small isolated fault. J. Struct. Geol. 93, 17–28. doi:10.1016/j.jsg.2016.10.002.

Zoback, M., Zinke, J., 2002. Production-induced normal faulting in the valhall and ekofisk oil fields. Pure Appl. Geophys. 159, 403–420. doi:10.1007/978-3-0348-8179-1_17.

Zoback, M.D., Gorelick, S.M., 2012. Earthquake triggering and large-scale geologic storage of carbon dioxide. Proceedings of the National Academy of Sciences 109, 10164–10168. doi:10.1073/pnas.1202473109.
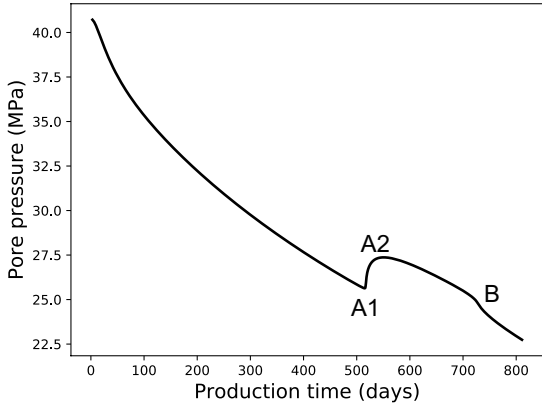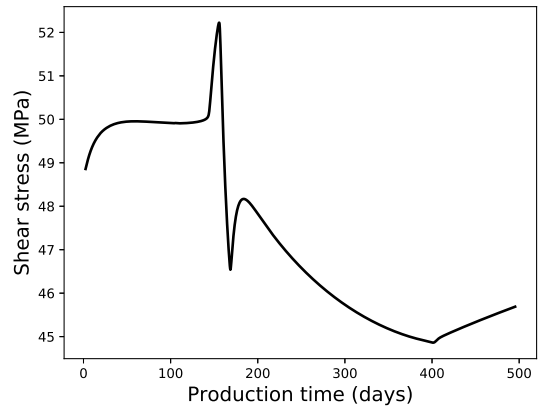
(a) Evolution of pore pressure on the left side of the fault.
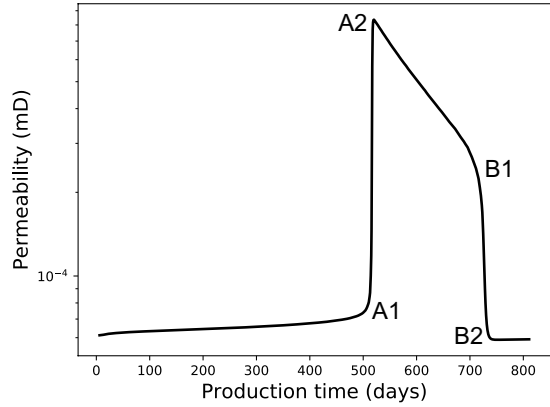
(b) Evolution of the fault permeability.
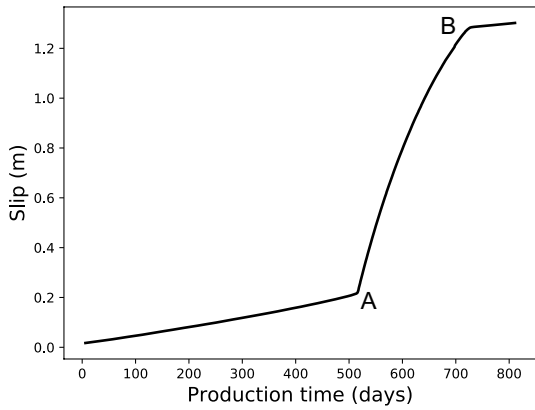
(c) Evolution of the fault slippage.
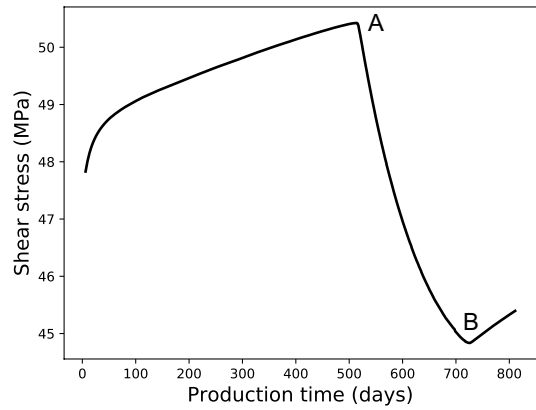
(d) Evolution of the fault shearing stress (Von Mises stress).
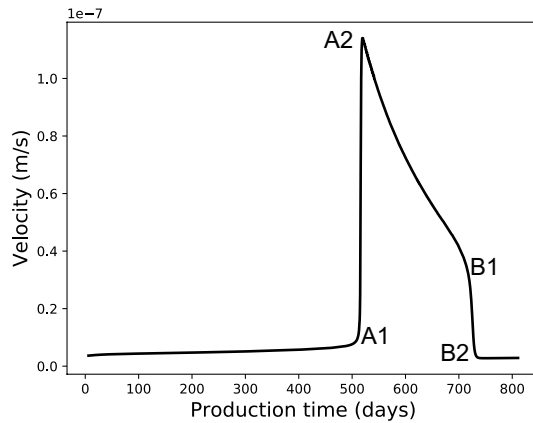
(e) Evolution of the fault slip rate.

Figure 21: Outputs of an event of chemical fault reactivation induced by reservoir production, following the setup of Sec. 7.1.
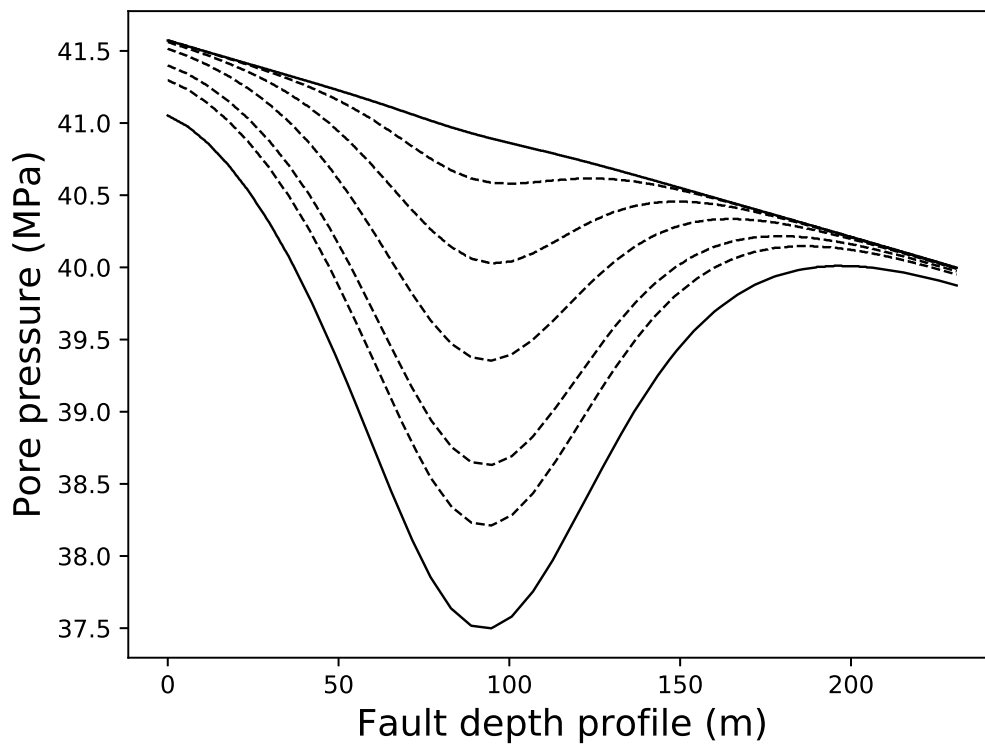
Figure 22: Profile of pore pressure along the fault reaching a steady shape during early production.
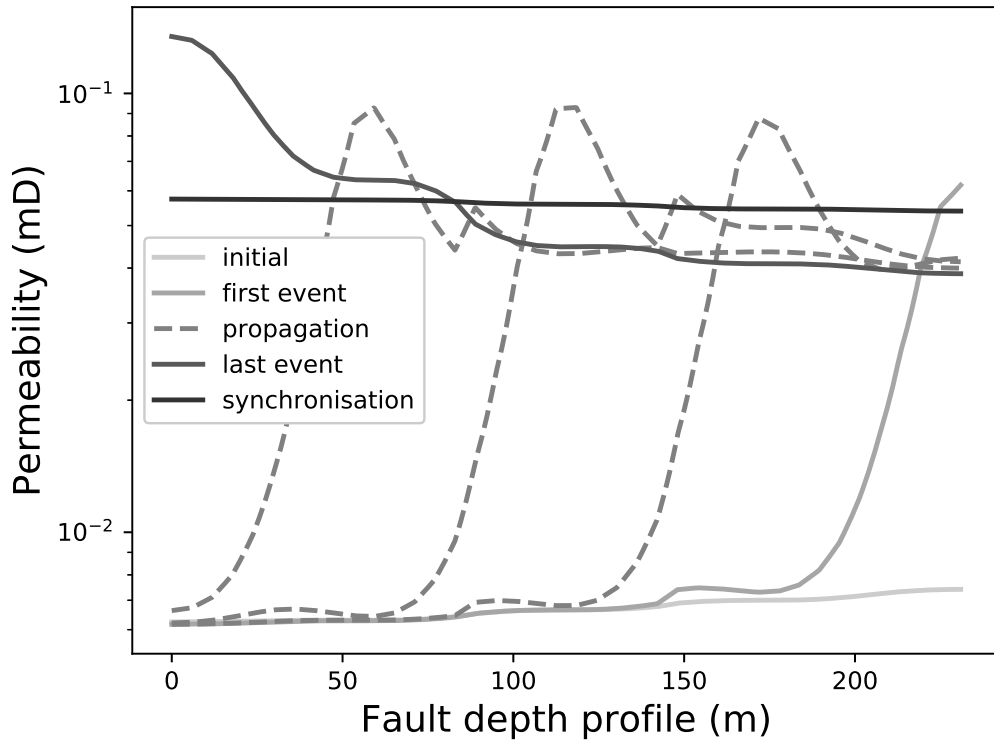
Figure 23: Profile of permeability along the fault before the first slip event until the full synchronisation of the fault.
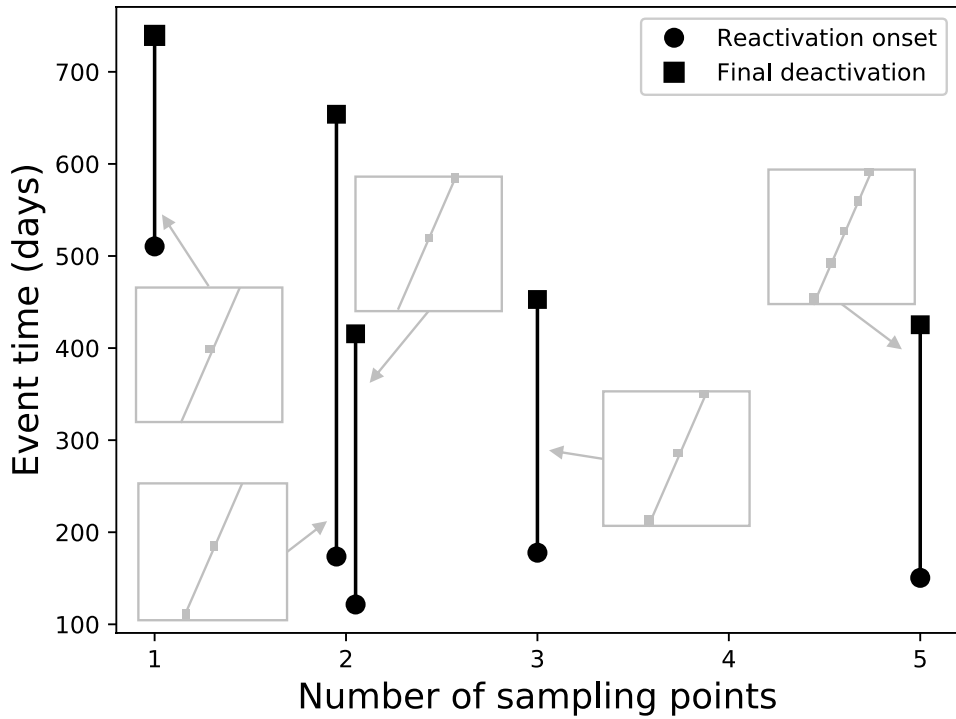
Figure 24: Fault reactivation occurrence and duration depending on number of sampling points considered. Points location along the fault are visualised in grey. Note that for the one sampling point simulation, only the middle point configuration leads to the fault reactivation.
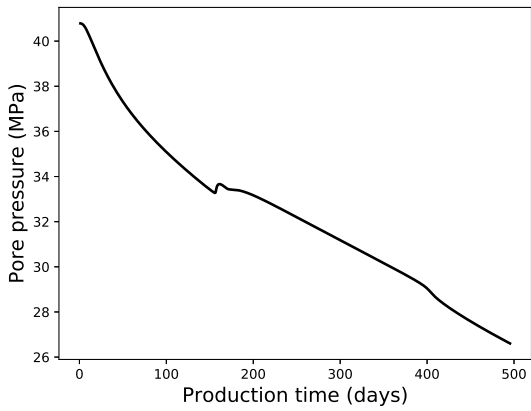
(a) Evolution of pore pressure on the left side of the fault.
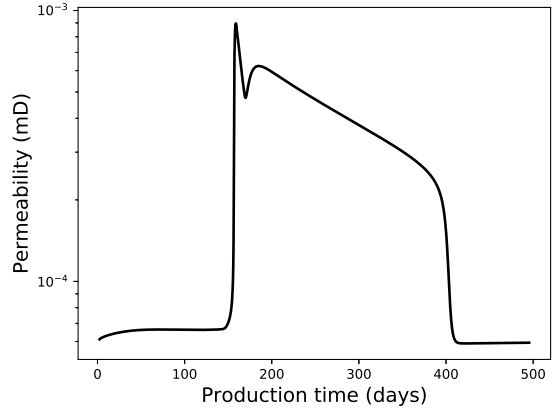
(b) Evolution of the fault permeability.
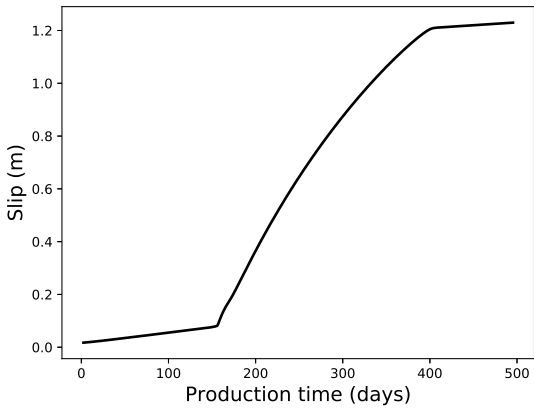
(c) Evolution of the fault slippage.

(d) Evolution of the fault shearing stress (Von Mises stress).
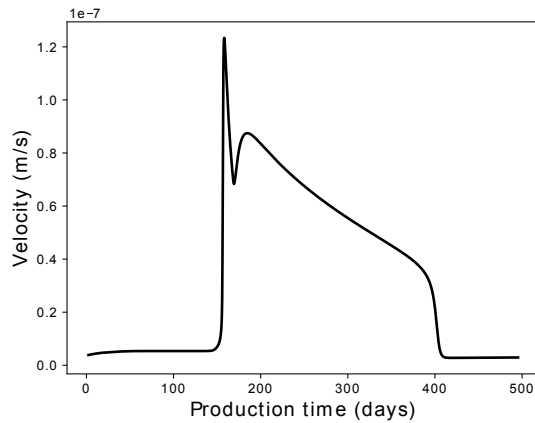
(e) Evolution of the fault slip rate.

Figure 25: Monitoring of the middle of the fault during a chemical fault reactivation induced by reservoir production, following the setup of Sec. 7.1 with five sampling points along the fault, referring to the final case of Fig. 24.
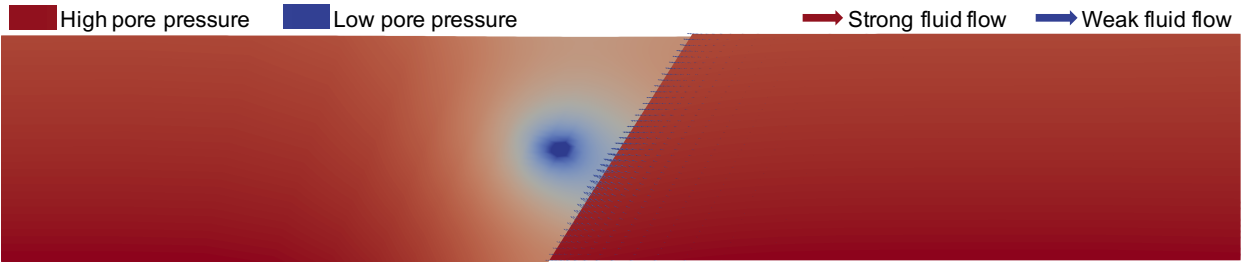
(a) Early stages of production
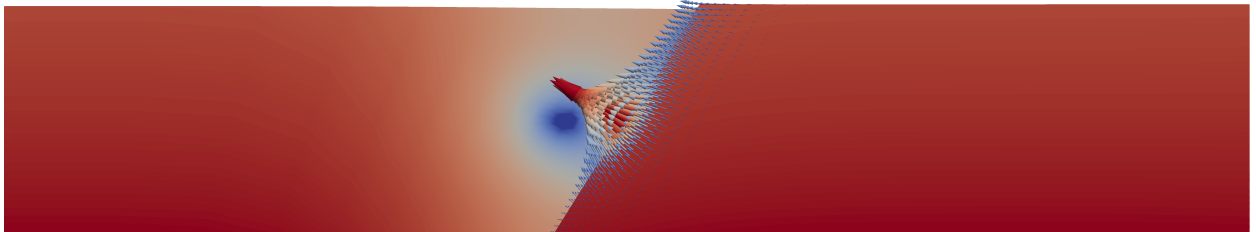
(b) Propagation to the middle of the fault. Contrary to the bottom segment, the top segment has already reactivated as shown by the difference of fluid velocity arrows size.
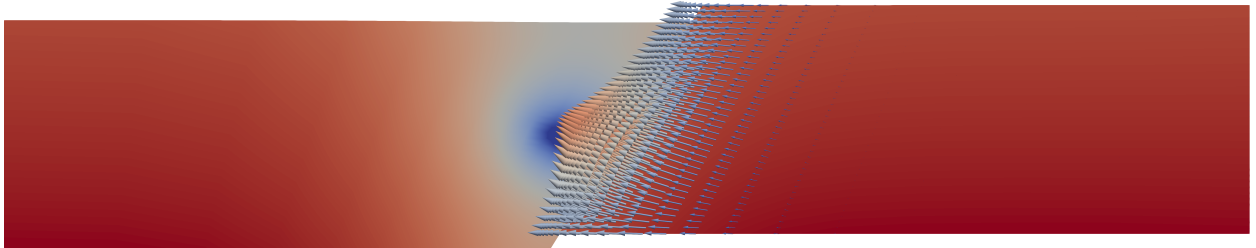
(c) Synchronisation of the whole fault
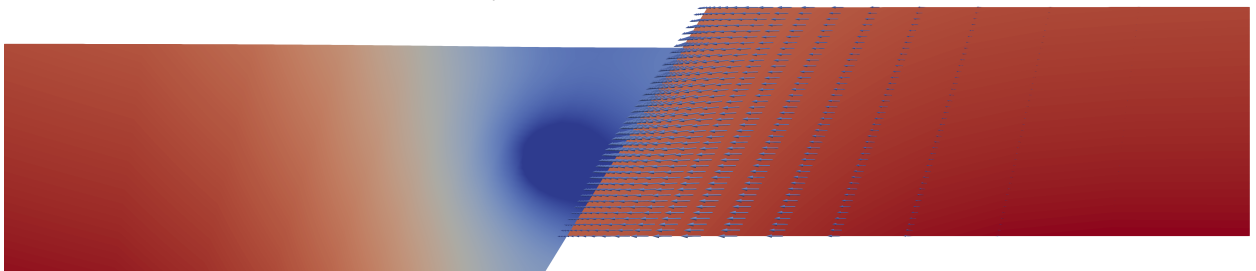
(d) Final state after fault deactivation and healing

Figure 26: Pressure distribution in the reservoir and fluid velocity in the right-hand-side compartment at different times during the reactivation event. The arrows size is proportional to the magnitude of the fluid velocity. Displacements are magnified by 30 times for visualisation purposes. The effect of the reactivation and corresponding permeability increase is observed on the pressure depletion across the fault.
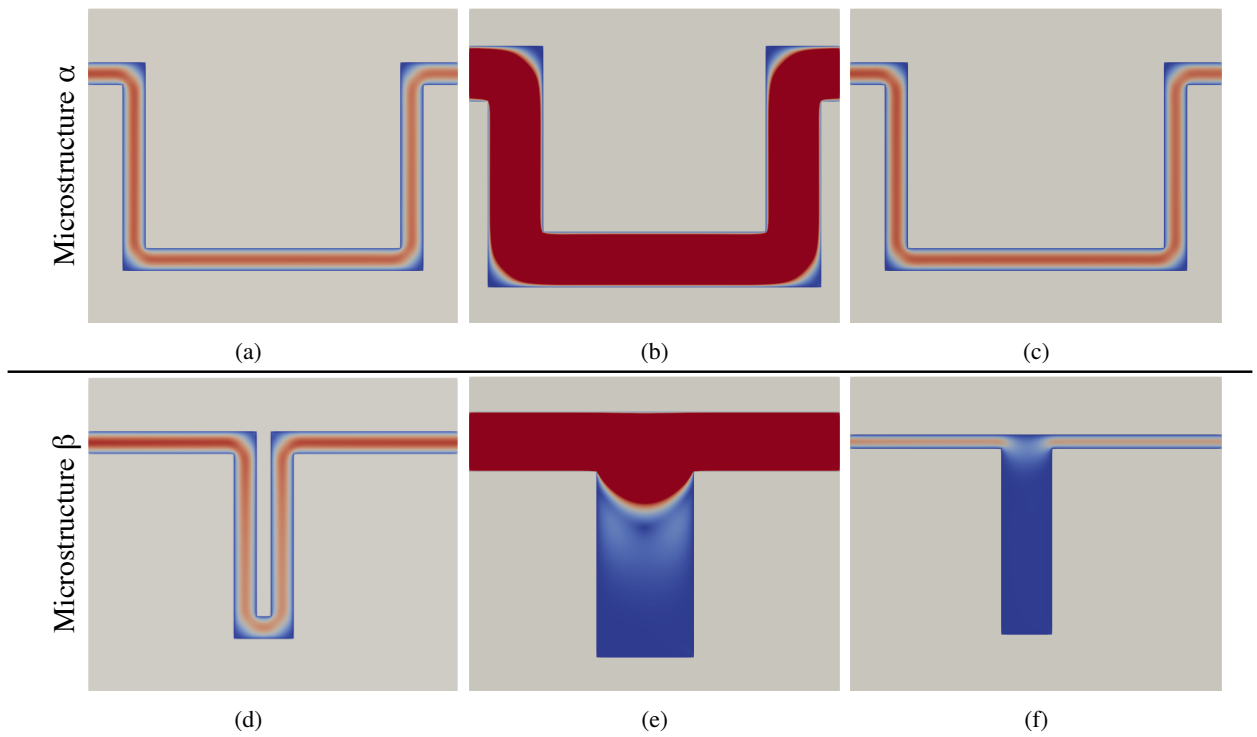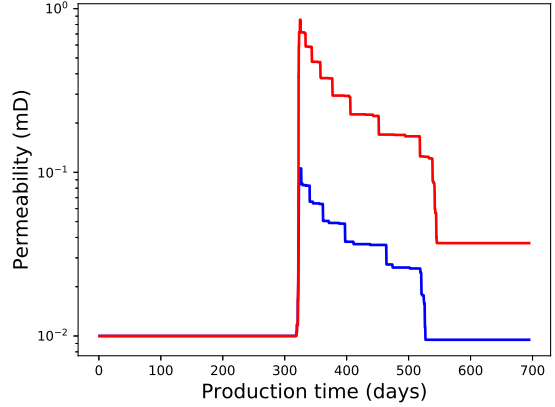
Figure 27: Initial state, peak dissolution and final reprecipitation (left to right respectively) of two different microstructures (α on top and β at the bottom) for the case study of Sec. 7.1.
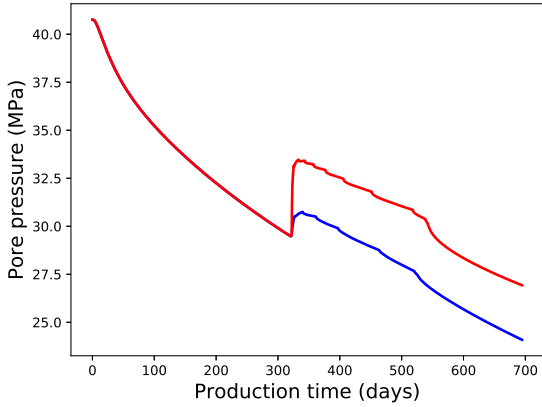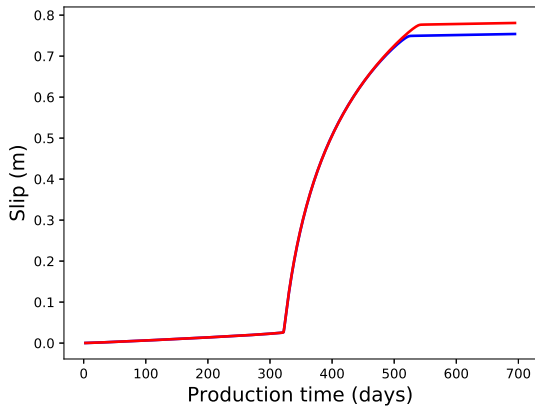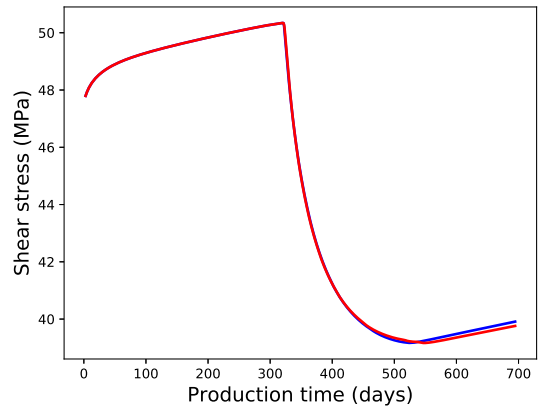
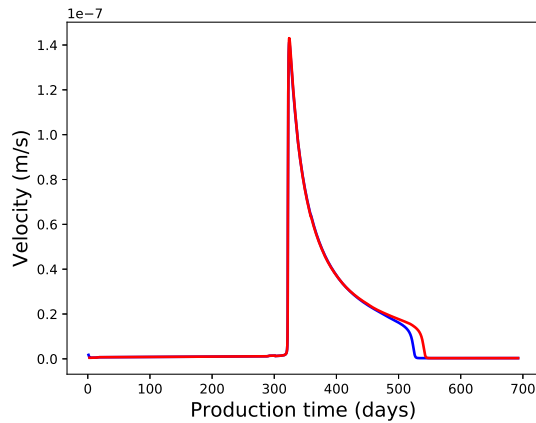(a) Evolution of pore pressure on the left side of the fault.

(b) Evolution of the fault permeability.

(c) Evolution of the fault slippage.

(d) Evolution of the fault shearing stress (Von Mises stress).

(e) Evolution of the fault slip rate.

Figure 28: Outputs during a reservoir production following the setup of Sec. 7.1. Blue curve corresponds to the microstructure A and red curve to microstructure B.